# A new stress measurement strategy based on time-frequency characteristics of Lamb waves

Hexin Cui [a], Zhichun Zhang [b], Hongbo Jia [c], Jiaze He [a,*], Yanju Liu [a,*], Jinsong Leng [b]

[a] Department of Astronautical Science and Mechanics, Harbin Institute of Technology (HIT), P.O. Box 301, No. 92 West Dazhi Street, Harbin 150001, People's Republic of China
[b] Center for Composite Materials and Structures, Harbin Institute of Technology (HIT), P.O. Box 3011, No. 2 Yikuang Street, Harbin 150080, People's Republic of China
[c] BYD Automotive Industry Co., Ltd., Shenzhen 518118, People's Republic of China

## ARTICLE INFO

## ABSTRACT

Existing stress evaluation methods based on the Lamb waves mainly use the time of flight (TOF) or velocity as the means of stress measurement. However, these two features used for stress measurement are sometimes insensitive to stress changes. Therefore, it is essential to explore other features that are potentially more sensitive to stress changes. The time–frequency spectrums of signals containing stress information have not yet been fully studied for stress evaluation. This paper proposes a uniaxial stress measurement method based on two time-–frequency characteristics of Lamb waves, i.e., the slope of time–frequency spectrum distribution (TFSD) and pulse width impact factor. Theoretical expressions of the slope of TFSD are derived. The impacts of excitation signal parameters (i.e., bandwidth and center frequency) and noise on two time–frequency characteristics were discussed. Then, the fitting results of the finite element simulation are consistent with the results predicted by theory. To experimentally validate the proposed theory, aluminum plate specimens with two different types of adhesives were used for the experiment. According to the experimental stress measurement expression, three uniaxial tensile tests in the range of 35–95 MPa were conducted on the identical batch of specimens. The maximum standard deviation of multiple measured stress based on pulse width impact factor is 3.76433 MPa, demonstrating excellent measurement stability. The maximum standard deviation of multiple measured stress based on the slope of TFSD is 9.12492 MPa. It shows that the proposed methodology is a promising alternative for stress measurement.

## 1. Introduction

Numerous large-scale engineering equipment are subjected to cyclical loads and harsh service environments during operation. Undergoing long-term service, critical structural components will experience stress concentration and redistribution. If the stress level surpasses the intended design value or fatigue accumulates to a critical level, it can lead to macroscopic cracks and potentially catastrophic failures. These failures could manifest suddenly as fractures in aircraft wings, leakages in oil or natural gas pipelines, deformations in high-pressure vessels, or cracks in high-speed rail infrastructure [1–4]. Therefore, accurate stress measurement and characterization techniques in structural components are crucial to ensuring the safety of human life and property [5,6]. After many years of development, two categories of stress detection methods have been formed-destructive and nondestructive methods [7,8].

Without causing additional damage, the nondestructive methods implement stress measurements based on the variation of stress-related physical parameters. Among the nondestructive methods, ultrasound-based stress measurement is one of the most attractive methods because of its advantages of directional transmission, fast detection, and wide measurement range [9].

The ultrasonic stress measurement methods have rapidly developed since the acoustoelastic effect of bulk waves was first proposed and experimentally verified by Hughes and Kelly [10]. They implemented Murnaghan's theory to describe the nonlinear changes in the structure's constitutive relation under static loading to study the dependence of ultrasonic wave velocity on the applied load. The ultrasonic wave velocity was found to be linearly related to the load in the linear elasticity range [11]. Therefore, the time-of-flight (TOF) or velocity of the ultrasonic wave is commonly used as a feature for stress measurement

[12,13]. Among approaches using bulk waves, longitudinal critically refracted (LCR) wave is one of the most popular stress measurement methods due to the highest sensitivity to uniaxial stress [14–16]. He et al. [17] placed a transmitter transducer and two receiver transducers on the steel plate to measure the average stress in a small region based on the TOF difference of the LCR waves obtained from the experiment. However, TOF and velocity are only two features from the plentiful information in the received signals. These two features are known to be easily distorted by environmental factors (e.g., noise), resulting in low detection reliability. Spectrum analysis appeared at the right time to enrich ultrasonic stress detection methods, which can provide the frequency-domain characteristics of signals [18,19]. Li et al. indicated the linear relationship between the inverse of characteristic frequency (CF) and uniaxial stress. Using the calibrated parameters, the uniaxial stress in a steel block has been evaluated by extracting the CF from the pulse-echo signals of shear waves [20]. However, with the growing demand for online stress monitoring in engineering, many researchers have focused their attention on Lamb waves in recent years to expand the evaluation range and enhance the accuracy of ultrasonic stress estimation.

Husson [21] first introduced acoustoelastic theory into Lamb waves to investigate the dependence of group or phase velocity on applied stress. Gandhi et al. [22,23] derived the acoustoelastic equation for Lamb waves under biaxial stress. They discovered the linear correlation between the phase velocity changes and uniaxial stress. Meanwhile, the linear relationship was verified by simulation and experiment, which provides theoretical guidance for Lamb waves stress monitoring based on the phase velocity changes [24,25]. Shi adopted the TOF ratio of A0 wave and S0 wave at a single frequency as the feature to evaluate stress. This strategy efficiently eliminates the impact of the distance between pitch-catch transducers on the stress calibration coefficient [26]. Shi et al. [27] proposed a method for estimating arbitrary biaxial stress by measuring the changes in phase velocity and conducted an experimental study based on piezoelectric transducer arrays. Pei [28] analyzed the effect of applied stress on high-order Lamb waves. Compared to other modes, the S1 mode demonstrates a higher sensitivity to stress in its group velocity change, enhancing the ability for stress measurement.

For complex structures with arbitrary cross-sections, theoretical methods cannot obtain the dispersion curves under varied stress levels. Researchers established a semi-analytical finite element method to obtain the relationship between ultrasonic velocity and stress for selecting the mode-frequency pair most sensitive to stress [29–34]. To avoid the influence of human factors on signal feature extraction, Lim et al. [35] directly used the time-domain response as input to a convolutional neural network to estimate dynamic stress.

As seen from the above research, existing stress evaluation methods utilizing the Lamb waves primarily rely on TOF or velocity for stress measurement. However, these two features used for stress evaluation exhibit limited sensitivities to stress [28]. Therefore, it is essential to explore other features that are potentially more sensitive to stress changes. The time–frequency domain of the signal also contains much useful information. Pai et al. [36] indicated that the time-varying frequencies can be used to distinguish whether the Lamb waves propagating inside a flat plate are symmetric or antisymmetric modes. In addition, they found that the interaction of two different waves leads to peaks in the time–frequency curve, a feature that can be used for damage detection. Hua et al. [37] extracted frequency-velocity ridge from time-frequency spectrums and used ridge curvature as a damage index for corrosion damage which is independent of distance. Moreover, they also proposed the difference coefficient between the time–frequency images as an effective damage index for damage identification, free of reference signals. Rizvi et al. [38] proposed three time–frequency damage indices, namely the energy concentration of the time–frequency distribution, time–frequency flux, and instantaneous frequency. Based on these three time–frequency indices, they trained a regression model to predict crack size precisely. In addition to damage information, the time–frequency

spectrums of the signals also contain stress information. Thus, this paper explores a stress measurement method based on multiple time–frequency features to enrich stress monitoring strategy and enhance the reliability of the detection results. The remaining sections of this paper are structured as follows: Firstly, the dispersive wave packets model is introduced, which is the theoretical basis for calculating the time-frequency characteristics. Then, the theoretical derivation of time-frequency characteristics of the response signal is given. At the same time, The impacts of excitation signal parameters (i.e., bandwidth and center frequency) and noise on two time–frequency characteristics were discussed. Subsequently, a finite element model is established to obtain ideal Lamb wave response signals without the effects of adhesive or noise. Then, aluminum plate specimens with two different types of adhesives were used for the experiment. The effect of adhesive on stress measurement factor is analyzed. Simultaneously, three uniaxial tensile tests in the range of 35–95 MPa were conducted on the identical batch of specimens to verify the feasibility of the proposed approach. Ultimately, the conclusion and future studies related to this method are pointed out.

## 2. Theoretical background

### 2.1. Dispersive wave packets model

Using the Gabor pulse as the excitation signal and considering the quadratic dispersion, Jia et al. [39] provided a theoretical model comprising five parameters to describe wave packets in dispersive guided wave propagation. These parameters depict diverse signal characteristics, and subsequently in the paper, they are proposed to be applied to stress evaluation.

First, this theoretical model is briefly reviewed. When the excitation signal generates from the origin, $x = 0$, this time-domain wave packets can be depicted by

$$f(t) = m(t)e^{i\omega_0 t} \,, \tag{1}$$

where $m(t)$ is the envelope function of an excitation signal, and $\omega_0$ represents the specific frequency of the excitation signal. When a single mode wave travels to a position $x$, the waveform expression for this 1D propagation is shown as

$$f(x,t) = \frac{1}{2\pi} \int_{-\infty}^{\infty} M(\omega - \omega_0)e^{i(\omega t - kx)}d\omega \,, \tag{2}$$

where $M(\omega) = \int_{-\infty}^{\infty} m(t)e^{-i\omega t}dt$, $\omega$ is angular frequency, $k$ represents the wavenumber and is a function of $\omega$ for this single mode wave. This function represents the dispersion relation, denoted by the symbol $K(\omega)$ in this paper. For describing the wave propagation, the dispersion relation is approximately replaced by Taylor expansion near the specific frequency $\omega_0$

$$k \equiv K(\omega) = k_0 + k_1(\omega - \omega_0) + k_2(\omega - \omega_0)^2 + \cdots \,, \tag{3}$$

where $k_j (j = 0, 1, 2)$ represent the coefficients in front of the Taylor expansion terms of the wavenumber near the specific frequency $\omega_0$. To describe the nonlinear dispersion effect of wave propagation, the Taylor expansion is retained in the second-order approximation solution. According to Taylor expansion theory, we know $1/k_1 = d\omega/dk$, which is the expression of group velocity, represented as $c_g$. By employing $c_g$ as a variable, the expression for $k_2$ becomes $-c_g'/(2c_g^2)$, where the prime signifies the derivative with respect to $\omega$. Then, substituting Equation (3) into Equation (2) yields

$$f(x,t) = 1/(2\pi) \times e^{-ik_0 x} \int_{-\infty}^{\infty} \left[ M(\omega - \omega_0)e^{-ik_1 x(\omega - \omega_0)} \right]$$
$$\times \left[ e^{-ik_2 x(\omega - \omega_0)^2} \right] e^{j\omega t}d\omega. \tag{4}$$

Equation (4) can be understood as the inverse Fourier transform

(IFT) of the product of two Fourier transforms, distinguished by the square brackets in the integral.

The IFT of the expression in the first square brackets is $m(t - k_1 x)$ and the IFT of the expression in the second square brackets is

$$q(t) = \sqrt{\alpha/\pi}\exp(-\alpha t^2) ,\tag{5}$$

where $\alpha = (4ik_2 x)^{-1}$. Applying the convolution theory, the Equation (4) becomes

$$f(x,t) = [m(t - k_1 x) \otimes q(t)]\exp[i(\omega_0 t - k_0 x)] ,\tag{6}$$

where $\otimes$ represents convolution. Let $\tau = k_1 x$, where $\tau$ denotes the TOF of the wave packet. Therefore, the Equation (6) can be further written as

$$f(\tau,t) = [m(t - \tau) \otimes q(t)]\exp[i\omega_0 \cdot (t - \tau) + i\phi'] ,\tag{7}$$

where $\phi' = (\omega_0 - k_0/k_1)\tau$.

In this study, the modulated Gaussian pulse with a center frequency $2\pi f_c$ was selected as the excitation signal

$$e(t) = A\exp(-t^2/2s^2)\cos(2\pi f_c t) ,\tag{8}$$

where the $A$ represents the amplitude, $s$ represents the pulse width factor, which determines the time span of the pulse waveform. The selection of $\omega_0$ is generally made to match a point where there is high wave energy intensity in the excitation signal. The frequency of the high wave energy intensity point in this excitation signal is the center frequency. Therefore, specific frequency $\omega_0$ equals to $2\pi f_c$, and $m(t)$ in the Equation (1) becomes the envelope function of $e(t)$. The expression of $m(t)$ can be written as

$$m(t) = A\exp(-t^2/2s^2).\tag{9}$$

Substituting the expressions of $\omega_0$ and $m(t)$ into the Equation (7), the time-domain waveform expression can be derived as

$$f(\tau,t) = \sqrt{(g_1(\tau) - ig_2(\tau)/\beta)}\exp\left[-(t-\tau)^2\beta g_1(\tau)\right]\exp\left\{i\left[2\pi f_c \cdot (t-\tau)\right.\right.$$
$$\left.\left. + g_2(\tau)\cdot(t-\tau)^2 + \phi'\right]\right\} ,\tag{10}$$

where $\beta = 1/2s^2$, $g_1(\tau)$ and $g_2(\tau)$ are the functions of the propagation time $\tau$, containing the expansion coefficients $k_j (j = 1, 2)$. The mathematic expressions of $g_j(\tau)(j = 1, 2)$ are

$$g_1(\tau) = k_1^2/(k_1^2 + (4\beta\tau k_2)^2); g_2(\tau) = 4\beta^2\tau k_2 k_1/(k_1^2 + (4\beta\tau k_2)^2).\tag{11}$$

We can see that the amplitude and phase in time-domain waveform expression are the function of the propagation time $\tau$. To simplify the analysis, amplitude and phase are considered as TOF-independent constants. Therefore, a parametric wave packet model considering nonlinear dispersion can finally be obtained

$$v(\Theta;t) = \xi\exp\left[-\beta\delta\cdot(t-\tau)^2\right]\cos\left[2\pi f_c\cdot\left(c\cdot(t-\tau)^2 + (t-\tau)\right) + \varphi\right] ,\tag{12}$$

where $\Theta = [\xi \delta \tau\ c\ \varphi]$. All the parameters for describing the dispersive waveform are included in the vector $\Theta$, where $\xi$ represents the amplitude, $\delta$ represents the pulse width impact factor, $\tau$ represents the TOF, $c$ represents the mode characteristic constant, and $\varphi$ represents the phase. Here, the expression of $c$ equals to $g_2(\tau)/2\pi f_c$ and $\delta = g_1(\tau)$. Thus, the Equation (11) can be rewritten as

$$\delta = k_1^2/(k_1^2 + (4\beta\tau k_2)^2); 2c\pi f_c = 4\beta^2\tau k_2 k_1/(k_1^2 + (4\beta\tau k_2)^2).\tag{13}$$

The specific physical meaning of $\delta$ will be explained in the next section.

## 2.2. Theoretical derivation of time–frequency characteristics of response signal

### 2.2.1. Time-frequency characteristics of the received signals

The time–frequency analysis technology maps the time-domain signals to the time–frequency domain, comprehensively reflecting the time–frequency characteristics of the time-varying signals. For stress measurement, previous work has studied the influence of stress on the time-domain characteristics (amplitude, phase, and TOF) of Lamb waves. In addition, some research has also explored the impact of stress on the frequency-domain characteristics of Lamb waves. However, these single-dimensional analyses, such as time-domain analysis or frequency-domain analysis, cannot fully utilize the information in the Lamb waves. Time-frequency analysis, on the other hand, can reflect the energy distribution with respect to both frequency and time. Therefore, exploring the relationship between the features of the time–frequency domain and stress is meaningful.

Two time–frequency characteristics of Lamb wave signals are introduced for stress measurement in this paper. To more intuitively display their physical meaning, a synthetic time-domain signal with a propagation distance of 300 mm at 100 MPa uniaxial stress can be obtained from the dispersive wave packet model (illustrated in Fig. 1 (a)). By employing the Wigner-Ville transformation, one can obtain the time–frequency spectrum of the signal.

Two essential features (i.e., the TFSD and the pulse width) in the time–frequency domain of the Lamb waves are shown in Fig. 1 (b). Among them, the dash-dotted line represents the distribution of frequency with time, whose slope at center frequency denotes how fast the frequency changes with time. We call it the slope of TFSD. A symbol $H(\sigma)$ is used to represent the slope of TFSD. Here, $\sigma$ represents stress. Another time–frequency characteristic is pulse width, which is represented by a dashed line in Fig. 1 (b) and denotes the time span of the signal. The wave packet parameter $\delta(\sigma)$ obtained by the dispersive wave packets model is called the pulse width impact factor. The expansion of Lamb wave pulse width caused by dispersion is represented by $\delta(\sigma)$. Therefore,
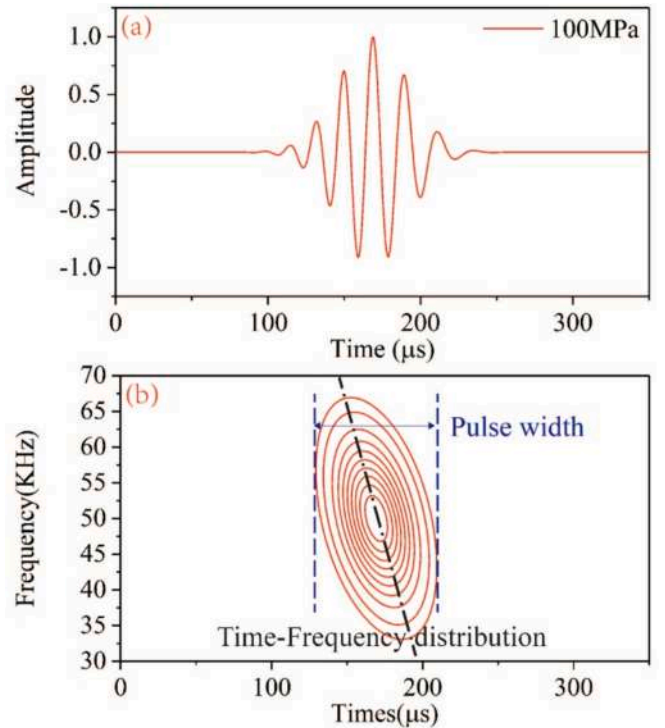


**Fig. 1.** Time-Frequency feature of Lamb waves: (a) time-domain waveform at 100 MPa, (b) time–frequency result obtained by Wigner-Ville transformation of the time-domain waveform in figure (a).

this paper expects to use $H(\sigma)$ and $\delta(\sigma)$ to achieve stress measurement in this paper.

### 2.2.2. Theoretical derivation of the slope of TFSD

To calculate the value of $H(\sigma)$ at each stress level, the theoretical expression of the slope of TFSD needs to be derived. Firstly, we must derive the analytical expression of TFSD. This paper defines the curve formed by connecting the TOF corresponding to the highest energy value of each frequency component as the affine curve. The affine curve completely coincides with the TFSD. When an A0 mode travels to the position $x$, the analytical expression of the affine curve can be obtained by mapping the group velocity dispersion curve

$$t = x/v_g(\omega) , \qquad (14)$$

where $v_g(\omega)$ represents the group velocity dispersion curve of the A0 mode, which depicts the relationship of group velocity with frequency. Fig. 2 is a schematic diagram illustrating how an affine curve is obtained by mapping the group velocity dispersion curve. The affine curve is a function of time and frequency, while the group velocity dispersion curve is a function of velocity and frequency. From Fig. 2, it can be observed that for a given frequency point $\omega$, we can calculate the corresponding time point t using $t = x/v_g$. Thus, by applying an affine transformation to each frequency point on the group velocity, we can obtain the entire affine curve. Therefore, if we know the expression of the group velocity dispersion curve $v_g(\omega)$, we can obtain the analytical expression of the affine curve through affine transformation. In conclusion, to determine the analytical expression of the affine curve, it is necessary to first understand the expression of the group velocity dispersion curve, and then use the affine transformation relationship to convert the relationship between frequency and velocity into a relationship between frequency and time.

This paper assumes that the group velocity curve of the A0 wave within the available frequency range (AFR) can be approximately presented by a linear fitting equation (as shown in Fig. 3 (b))

$$v_g(\omega) = v'_g\omega + b , \qquad (15)$$

where $v'_g$ is the slope of the linear equation. Substituting Equation (15) into Equation (14) yields the expression of the affine curve as

$$\omega = 1/v'_g(x/t - b). \qquad (16)$$

Let $\tau$ be the TOF of the A0 wave. The slope of the affine curve at $t = \tau$ represents the slope of TFSD. Therefore, by differentiating $\omega$ with respect to $t$, one can derive the expression for $H(\sigma)$,

$$H(\sigma) = d\omega/dt|_{t=\tau} = -v_{gc}/(\tau v'_g) , \qquad (17)$$

where $v_{gc}$ represents the group velocity of the A0 wave with the center frequency component. The relationship between $k_1$ and $k_2$ can be derived from the Equation (13)

$$k_2 = (2\pi f_c c)/(4\beta^2\tau\delta) \times k_1. \qquad (18)$$

By combining the relation of $k_1 = (v_{gc})^{-1}; k_2 = -v'_g/(2*v^2_{gc})$, we can obtain

$$v'_g = -(\pi f_c c)/(\beta^2\tau\delta) \times v_{gc}. \qquad (19)$$

By substituting the above equation into Equation (17), the expression of $H(\sigma)$ can be further obtained

$$H(\sigma) = (\beta^2\delta)/(\pi f_c c). \qquad (20)$$

It can be found that the value of $H(\sigma)$ is determined by the wave packet parameters $\delta$ and $c$. Therefore, combining the dispersive wave packet model with a parameter estimation algorithm can quickly obtain the value of $H(\sigma)$ from time-domain Lamb wave packet.

This paper considers the zero-stress state as the initial state. Therefore, the variation of the slope of TFSD $\Delta H(\sigma)$ induced by stress equals $H(\sigma)$ under every stress level minus $H(\sigma = 0)$ of the initial state. The expression of $\Delta H(\sigma)$ is as follows

$$\Delta H(\sigma) = (H(\sigma) - H(\sigma = 0)) , \qquad (21)$$

We use $\Delta H(\sigma)$ as a stress measurement factor and calibrate the linear equation between $\Delta H(\sigma)$ and stress.

In addition, the expression of the pulse width impact factor $\delta(\sigma)$ has been shown in Equation (13). Which is

$$\delta(\sigma) = k_1^2/(k_1^2 + (4\beta\tau k_2)^2) \qquad (22)$$

It can be seen that $\delta(\sigma)$ is a function of the Taylor expansion coefficients $k_1$ and $k_2$. Therefore, as long as we know $k_1$ and $k_2$, the theoretical value of $\delta(\sigma)$ can be calculated. The variation of pulse width impact factor $\Delta\delta(\sigma)$ induced by stress can be obtained by $\delta(\sigma)$ under every stress level minus $\delta(\sigma = 0)$ of the initial state

$$\Delta\delta(\sigma) = (\delta(\sigma) - \delta(\sigma = 0)). \qquad (23)$$

This paper selects $\Delta\delta(\sigma)$ as another stress measurement factor. The linear correlation of $\Delta\delta(\sigma)$ with stress is also calibrated in the next part.

## 3. Theoretical calculation and discussion of the time–frequency characteristics

### 3.1. Theoretical calculation method of time–frequency characteristics

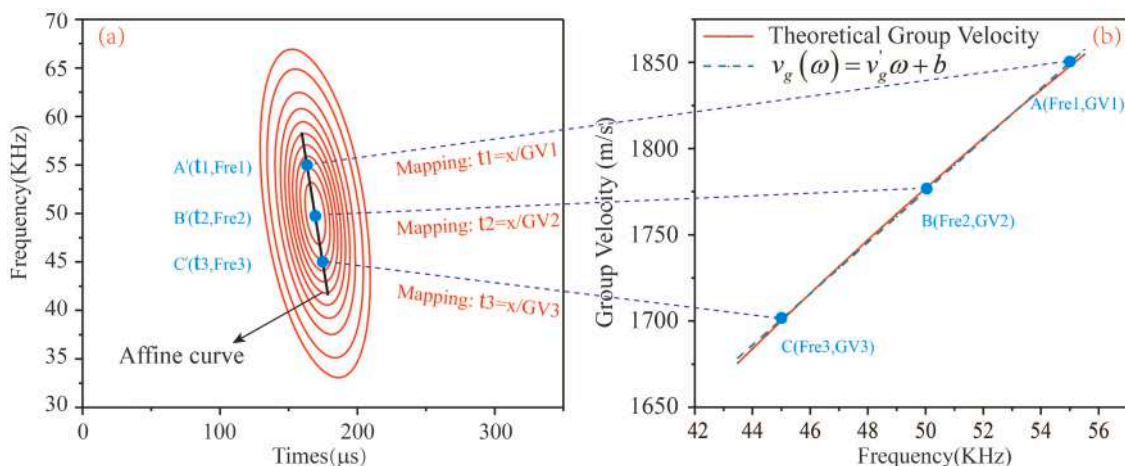To obtain the theoretical time–frequency characteristics proposed in



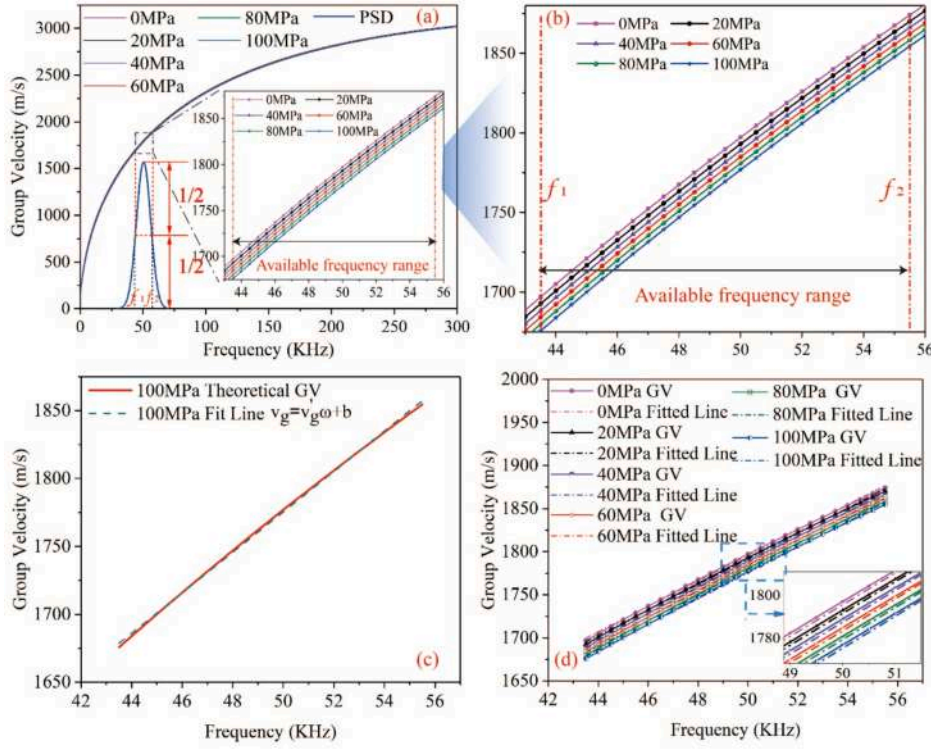Fig. 2. Affine transformation diagram: (a) affine curve, (b) group velocity dispersion curve.

**Fig. 3.** The method for calculating theoretical values of all parameters: (a) the dispersion curves of A0 mode Lamb waves under different stress states and PSD, (b) a magnified view of the AFR, (c) a fitted line of the dispersion curve in the AFR at 20 MPa, (d) all fitted lines of the dispersion curve within the AFR at 0 MPa, 20 MPa, 40 MPa, 60 MPa, 80 MPa, and 100 MPa.

the previous section, the group velocity curves under various stress conditions need to be acquired. The analytical expressions to predict the impact of uniaxial load on velocity were reported in detail by Gandhi *et al.* [23]. The dispersion relationship can be written as

$$D_{11}G_1\cot(\gamma\alpha_1) + D_{13}G_3\cot(\gamma\alpha_3) + D_{15}G_5\cot(\gamma\alpha_5) = 0 , \quad (24)$$

and

$$D_{11}G_1\tan(\gamma\alpha_1) + D_{13}G_3\tan(\gamma\alpha_3) + D_{15}G_5\tan(\gamma\alpha_5) = 0. \quad (25)$$

The Equation (24) represents symmetric modes and the Equation (25) is for antisymmetric modes. In the above two equations, $\gamma = \omega d/(2c)$, where $\omega$ represents the angular frequency, $d$ represents the plate thickness, and $c$ denotes the phase velocity along the $x_1$ axis. The symbols $\alpha_i(i = 1, 3, 5)$ represent the ratio of $x_3$ to $x_1$ wavenumbers. The parameters $G_m$ are given as

$$G_1 = D_{23}D_{35} - D_{33}D_{25} , \ G_3 = D_{31}D_{25} - D_{21}D_{35}, \\ G_5 = D_{21}D_{33} - D_{31}D_{23}. \quad (26)$$

The expressions of parameters $D_{ij}(i = 1, 2, 3; j = 1, 2...6)$ are given in Ref [23]. These two equations can be solved numerically to calculate the dispersion curves under different stress levels. The research object of this paper is only the antisymmetric fundamental mode, namely the A0 mode. Therefore, the dispersion curves of A0 mode Lamb waves under different stress states are presented in Fig. 3 (a). Taking an excitation signal with a central frequency of 50 KHz as an example, the pulse width factor of the excitation signal is $s = 20E-6$. the power spectral density (PSD) of the excitation signal is also shown in Fig. 3 (a). The frequency interval $[f_1, f_2]$ (shown in Fig. 3 (a)) corresponding to the half-maximum of PSD is defined as the available frequency range (AFR). Fig. 3 (b) is a zoomed-in view of the AFR, showing the group velocity curve in the AFR. It is found that group velocity curve changes accompanying the increment of stress. A linear equation (i.e., $v_g = v'_g\omega + b$) is used to approximate the group velocity curve of A0 mode in the AFR.

Furthermore, the Taylor expansion coefficients $k_1$ and $k_2$ can be obtained. Taking the dispersion curve at 20 MPa as an illustration, it is evident from Fig. 3 (c) that the linear fitted line adequately approximates the dispersion curve in the AFR. In Fig. 3 (d), the fitted lines from 0 to 100 MPa with a 20 MPa interval (Six fitted lines in total) are given to characterize the dispersion curves in the AFR. The calculation results indicate a regular change in the fitted lines with the increment of stress. It means that parameters calculated based on fitting coefficients may also change regularly accompanying the increment of stress.

To calculate theoretical values of $H(\sigma)$ and $\delta(\sigma)$, we need to obtain the parameters $v'_g, v_{gc}, \tau, k_1$ and $k_2$ under all stress levels. Among them, $v'_g$ can be obtained from the linear equation $v_g = v'_g\omega + b$. Parameter $v_{gc}$ is the group velocity of the central frequency component. Parameter $\tau$ is the TOF of the central frequency component, which can be obtained by the expression $\tau = x/v_{gc}$. Parameters $k_1$ and $k_2$ can be obtained by combining the relation of $k_1 = (v_{gc})^{-1}; k_2 = -v'_g/(2 * v^2_{gc})$. Substituting the parameters $v'_g, v_{gc}$ and $\tau$ into the Equation (17) can obtain the slope of the TFSD $H(\sigma)$ under all stress levels. Substituting the parameters $k_1$ and $k_2$ into Equation (22) can obtain pulse width impact factor $\delta(\sigma)$ under all stress levels. From the above calculation process, it can be observed that parameters $v'_g, v_{gc}, \tau, k_1$ and $k_2$ are influenced by the frequency range and central frequency of the excitation signal. Therefore, the next part will discuss the impact of the bandwidth and central frequency of the excitation signal on the accuracy of stress evaluation based on two time–frequency characteristics proposed in this paper.

### 3.2. The impact of the excitation signal

The accuracy of stress evaluation based on the two time–frequency characteristics is influenced by the parameters of the excitation signal, including the bandwidth and center frequency of the excitation signal.

### 3.2.1. The impact of excitation signal bandwidth on the accuracy of stress evaluation

The bandwidth of the excitation signal is controlled by the parameter $s$ (pulse width factor). To investigate the influence of the excitation signal's bandwidth on the accuracy of stress evaluation based on time–frequency characteristics, four excitation signals with a center frequency of 50 KHz are studied. Their pulse width factors are $s = 15E-6$, $s = 20E-6$, $s = 25E-6$, and $s = 30E-6$ respectively. Fig. 4 shows the power spectra density of these four excitation signals. It can be observed that with the increase in the pulse width factor $s$, the bandwidth of the excitation signal gradually decreases.

For excitation signals with different bandwidths, the two stress evaluation factors $\Delta H(\sigma)$ and $\Delta \delta(\sigma)$ under different stresses are calculated using the method described in the previous section. As shown in Fig. 5 (a) and (b), both stress measurement factors exhibit a linear relationship with stress even when using excitation signals with different bandwidths. The accuracy of stress evaluation based on time–frequency characteristics is defined as $\Delta H(\sigma)/MPa/H(\sigma = 0)$ ($\Delta \delta(\sigma)/MPa/\delta(\sigma = 0)$). The relationship between the accuracy of stress evaluation based on two time–frequency characteristics and the bandwidth of the excitation signal is shown in Fig. 5 (c) and (d). It can be observed that the accuracy of the stress measurement factor $\Delta H(\sigma)$ is not affected by the bandwidth of the excitation signal. For the stress measurement factor $\Delta \delta(\sigma)$, the accuracy of stress evaluation decreases as the bandwidth of the excitation signal decreases. Therefore, increasing the bandwidth of the excitation signal can improve the accuracy of stress evaluation based on the stress evaluation factor $\Delta \delta(\sigma)$.

### 3.2.2. The impact of excitation signal center frequency on the accuracy of stress evaluation

From Fig. 3 (a), it can be seen that for excitation signals with the same frequency range, the dispersion degree of the propagating wave gradually weakens as the center frequency of the excitation signal increases. Therefore, to discuss the influence of the propagating wave dispersion degree on the accuracy of stress evaluation based on two time–frequency characteristics. This section studied eight excitation signals with the same bandwidth (i.e., $s = 20E-6$), centered at frequencies ranging from 50 KHz to 190 KHz with a step size of 20 KHz.

Fig. 6 (a) and (b) display the two stress evaluation factors $\Delta H(\sigma)$ and $\Delta \delta(\sigma)$ under different stresses. It can be observed that even when the excitation signals have different center frequencies, both time–frequency characteristics still exhibit a linear relationship with stress. Following the definition in the previous section, the accuracy of stress evaluation based on two time–frequency characteristics is calculated.
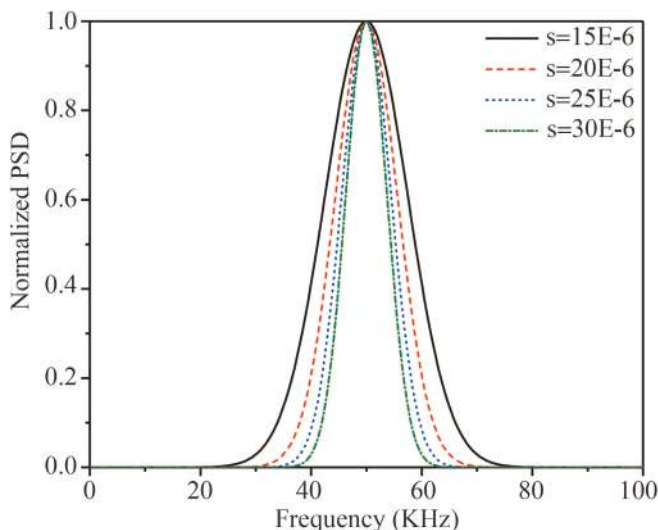
The relationship between the accuracy of stress evaluation based on two time–frequency characteristics and the center frequency of the excitation signal is shown in Fig. 6 (c) and (d). The accuracy of stress evaluation based on both time–frequency characteristics decreases as the dispersion degree of the propagating wave weakens.

Compared to $\Delta H(\sigma)$, the accuracy of stress evaluation using $\Delta \delta(\sigma)$ as a stress measurement factor is more severely affected by dispersion degree. Therefore, as the center frequency of the excitation signal increases, the bandwidth should be expanded to ensure the accuracy of stress evaluation when using $\Delta \delta(\sigma)$ as a stress measurement factor.

In addition, for the low dispersion degree of the propagating wave, the time–frequency characteristics proposed in this paper can still be used for stress evaluation. However, it is impractical in experiments due to the minimal variations in the two time–frequency characteristics. Therefore, in practical applications, choosing excitation signals that can generate a propagating wave with a higher dispersion degree is advisable. For example, within 200 KHz, the A0 mode can be selected, while above 300 KHz, the S0 mode can be chosen.

### 3.3. The impact of noise on the linearity of proposed time–frequency characteristics

To analyze the influence of noise on the stress evaluation based on two time–frequency characteristics, it is necessary to obtain time-domain signals with different intensity noise. Time-domain signals with noise are obtained by overlaying theoretical time-domain waveforms with Gaussian white noise. Theoretical time-domain waveforms under different stress levels can be reconstructed by combining the parameters ($\tau$, $k_1$ and $k_2$) with the dispersive wave packet model (Equation (11) and Equation (12)). The parameters $\tau$, $k_1$ and $k_2$ are listed in Table 1. White Gaussian noise (WGN) can be obtained by a MATLAB function wgn. This paper investigates the impacts of five types of noise intensities ($-20$ dB, $-25$ dB, $-30$ dB, $-35$ dB, and $-40$ dB) on the stress evaluation based on two time–frequency characteristics proposed in this paper. Fig. 7 shows the signals under zero stress, which are added with WGN of different intensities.

Time-domain signals with noise can be represented by the dispersive wave packets model (i.e., Equation (12)). Thus, combining the expectation–maximization (EM) algorithm with the dispersive wave packets model allows for the rapid acquisition of the wave packet parameter vector $\Theta = [\xi \delta \tau c \varphi]$ of Lamb wave signals under all stress levels.

The EM algorithm is implemented through two alternating steps. The first step is to calculate the probability distribution of hidden variables based on the initial estimates. That is the E-step; the second step is to utilize the probability distribution obtained in the E-step to maximize the likelihood function, which generates a new parameter vector. That is the M-step. Then, the parameters from the M-step are used to update the initial parameters in the E-step. After cyclic iteration, the estimated values of the parameter vector can be obtained. The specific implementation steps can be referenced in Jia's work [39]. Once the parameters corresponding to the wave packets at every stress state are extracted, the pulse width impact factor $\delta(\sigma)$ and the slope of TFSD are naturally obtained according to the Equations (22 and 20).

Generate twenty sets of Gaussian white noise with the same noise intensity randomly, and superimpose them on the theoretical reconstructed signals under any stress to form twenty signals. Thus, under each stress, twenty noisy signals are used to calculate twenty stress measurement factors $\Delta H(\sigma)$ or $\Delta \delta(\sigma)$. The mean and deviation of the twenty sets of $\Delta H(\sigma)$ ($\Delta \delta(\sigma)$) are calculated. Repeat the above calculation process for all stresses to obtain the influence of this noise intensity on the accuracy of stress evaluation using the two time–frequency characteristics. Thus, the impacts of different noise intensities on the stress evaluation using the two time–frequency characteristics are shown in Fig. 8.

In Fig. 8, the symbol represents the mean of twenty $\Delta H(\sigma)$ (or $\Delta \delta(\sigma)$). The Error bars represent the standard deviation. It can be seen that a
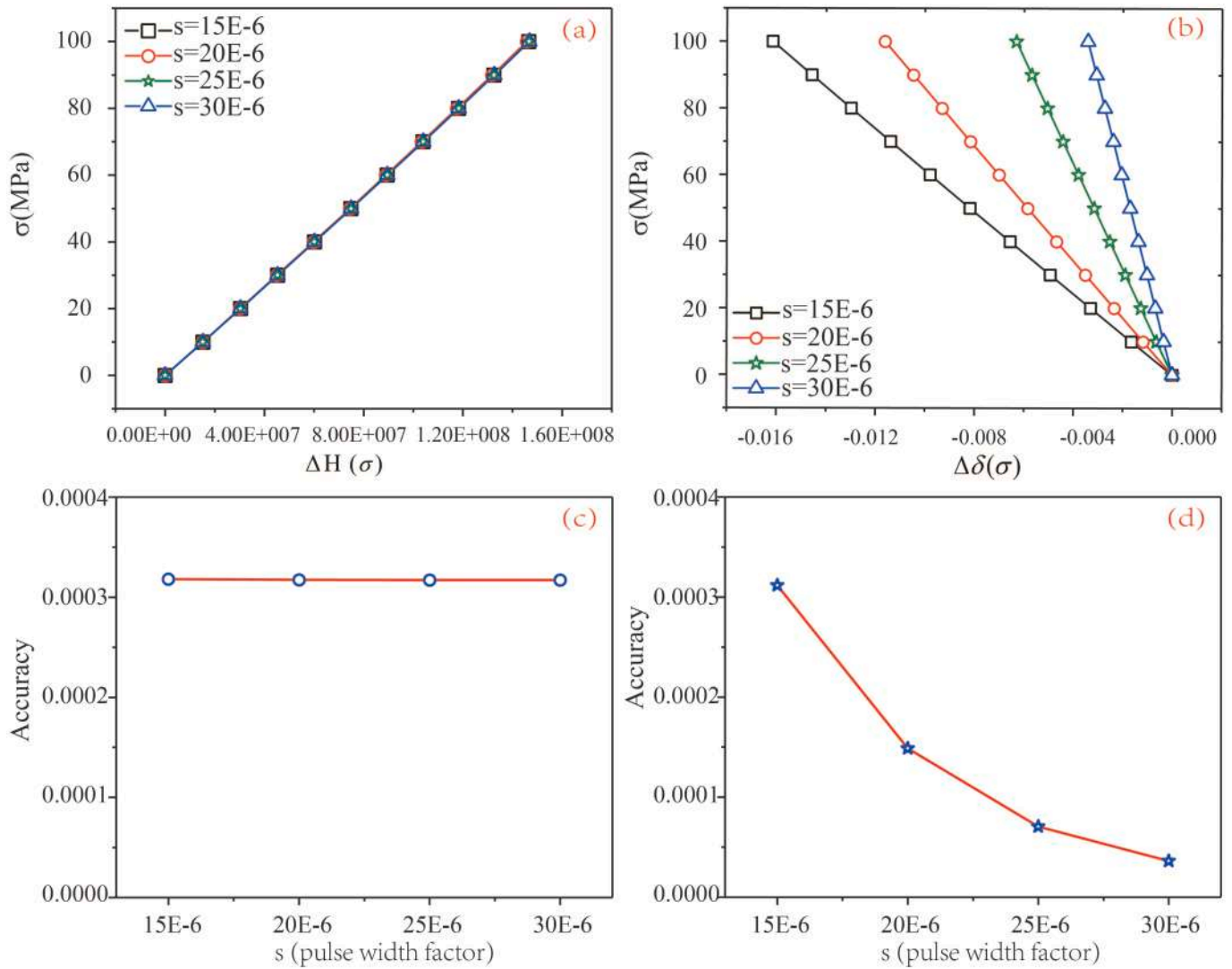


**Fig. 4.** PSD of the excitation signal with different pulse width factor.

**Fig. 5.** The influence of the bandwidth of the excitation signal: (a) and (b) The effect of the excitation signal bandwidth on the stress measurement factor $\Delta H(\sigma)$ and $\Delta\delta(\sigma)$ respectively. (c) and (d) The effect of the bandwidth of the excitation signal on the accuracy of stress assessment using $\Delta H(\sigma)$ and $\Delta\delta(\sigma)$ as the stress evaluation factor respectively.

significant level of noise intensity can affect the linearity and standard deviation of two time–frequency characteristics. As the noise intensity decreases, both the effects on linearity and standard deviation of the two time–frequency characteristics gradually decrease. For $\Delta H(\sigma)$, when the noise intensity is below $-35$ dB, its linearity and standard deviation are minimal. Compared to the characteristic $\Delta H(\sigma)$, the noise resistance performance of characteristic $\Delta\delta(\sigma)$ is slightly stronger, able to withstand noise levels below $-30$ dB.

### 3.4. Calibration of the theoretical stress measurement expression

To complete the calibration of the theoretical stress measurement expression, the theoretical values of the above two stress measurement factors are calculated under different stress levels in this section. Based on the previous analysis and discussion about the impact of the excitation signal, we choose a Gabor pulse in Equation (8) with $A = 1$, $f_c = 50$ KHz, and $s = 20E-6$ as the excitation signal. Fig. 9 (a) displays the time-domain wave packet of the excitation signal. Fig. 9 (b) exhibits the PSD of the excitation signal. The frequency range for half of the PSD is the available frequency region.

The study object of this paper is an aviation-specific aluminum plate with a thickness of 2 mm, belonging to the 2024 alloy. The material

exhibits a density of 2730 kg/m3, a Poisson's ratio of 0.34, and a Young's modulus of 73.1 GPa. The distance from the actuator to the receiving sensor is 300 mm. The applied stress varies in increments of 10 MPa, ranging from 0 to 100 MPa. By the theoretical calculation method introduced in Section 3.1, parameters $v'_g$, $v_{gc}$, $\tau$, $k_1$ and $k_2$ under all stress levels can be obtained and listed in Table 1. Moreover, Table 1 also contains the theoretical $H(\sigma)$ and $\delta(\sigma)$.

Using the parameters $\tau$, $k_1$ and $k_2$, theoretical time-domain waveforms under different stress levels can be reconstructed by the dispersive wave packet model. Fig. 10 (a) shows the theoretical time-domain waveforms obtained using Equation (12) from 0 to 100 MPa with a 20 MPa interval (six stress levels in total). We can see that the time delay in the time-domain waveform increases with the increment of stress. Fig. 10 (b) displays the TFSD of the response signals at stress levels of 20 MPa, 60 MPa, and 100 MPa. The straight line represents the tangent of the affine curve at $t = \tau$, and its slope is the slope of TFSD. The results exhibit the changes in the slope of TFSD accompanying the increment of the stress. In Fig. 10 (c), the pulse widths of the response signals under the stress levels of 20 MPa, 60 MPa, and 100 MPa, are given. It can be found that when the propagation distance is the same, the greater the stress, the more severe the time span of the wave packet expansion. It should be noted that the frequency range of TFSD displayed in Fig. 10
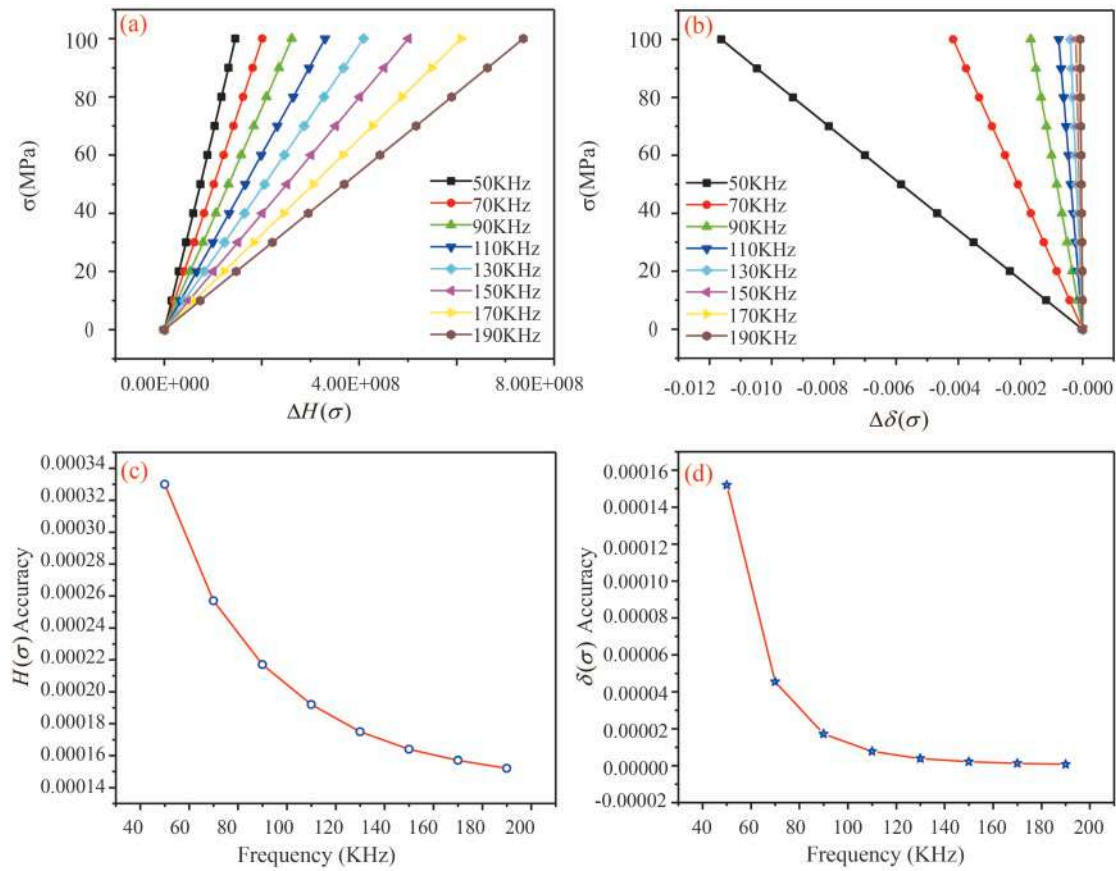
**Fig. 6.** The influence of the center frequency of the excitation signal: (a) and (b) The effect of the excitation signal center frequency on the stress measurement factor $\Delta H(\sigma)$ and $\Delta\delta(\sigma)$ respectively. (c) and (d) The effect of the center frequency of the excitation signal on the accuracy of stress assessment using $\Delta H(\sigma)$ and $\Delta\delta(\sigma)$ as the stress evaluation factor respectively.

**Table 1**
The theoretical values of all parameters under all stress levels.

| | $v_g'(10^{-3})$ | $v_g$ | $\tau(10^{-6})$ | $k_1(10^{-4})$ | $k_2(10^{-10})$ | $H(\sigma)(10^9)$ | $\delta(\sigma)$ |
|---|---|---|---|---|---|---|---|
| 0 MPa | 2.34657 | 1797.19918 | 166.92641 | 5.56892 | −3.63870 | −4.58813 | 0.77077 |
| 10 MPa | 2.34899 | 1795.15506 | 167.11648 | 5.57527 | −3.65077 | −4.57298 | 0.76960 |
| 20 MPa | 2.35138 | 1793.11479 | 167.30663 | 5.58163 | −3.66282 | −4.55797 | 0.76843 |
| 30 MPa | 2.35373 | 1791.07838 | 167.49685 | 5.58799 | −3.67484 | −4.54308 | 0.76726 |
| 40 MPa | 2.35605 | 1789.04586 | 167.68715 | 5.59435 | −3.68684 | −4.52831 | 0.76609 |
| 50 MPa | 2.35833 | 1787.01724 | 167.87751 | 5.60072 | −3.69882 | −4.51367 | 0.76493 |
| 60 MPa | 2.36059 | 1784.99253 | 168.06793 | 5.60708 | −3.71077 | −4.49916 | 0.76377 |
| 70 MPa | 2.36281 | 1782.97176 | 168.25841 | 5.61345 | −3.72270 | −4.48476 | 0.76261 |
| 80 MPa | 2.36499 | 1780.95494 | 168.44895 | 5.61982 | −3.73460 | −4.47049 | 0.76146 |
| 90 MPa | 2.36714 | 1778.94209 | 168.63955 | 5.62619 | −3.74648 | −4.45634 | 0.76030 |
| 100 MPa | 2.36925 | 1776.93322 | 168.83020 | 5.63257 | −3.75833 | −4.44232 | 0.75915 |

(b) and (c) is −6 dB bandwidth of the response signals for better observation, instead of the whole bandwidth.

Submitting the theoretical $H(\sigma)$ and $\delta(\sigma)$ into the Equation (21) and Equation (23) respectively, the values of $\Delta H(\sigma)$ and $\Delta\delta(\sigma)$ are calculated. A linear fit is used to characterize the functional relationship between stress $\sigma$ and $\Delta H(\sigma)$. The linear relationship obtained by fitting is, namely, the stress measurement expression. Similarly, calculating the fitted linear relationship between stress $\sigma$ and $\Delta\delta(\sigma)$ means completing the calibration of the stress measurement expression of the stress measurement factor $\Delta\delta(\sigma)$. Fig. 11 shows the theoretical calibration results for two stress measurement factors.

It is evident that a good linear correlation between the two stress measurement factors and stress. Fig. 11 (a) gives the theoretical stress measurement expression when selecting $\Delta H(\sigma)$ as a stress measurement factor

$$\sigma = 6.85757E - 7 \times \Delta H(\sigma) - 0.63506. \quad (27)$$

Fig. 11 (b) gives the theoretical stress measurement expression when selecting $\Delta\delta(\sigma)$ as a stress measurement factor

$$\sigma = -8605.10129 \times \Delta\delta(\sigma) - 0.14427. \quad (28)$$

## 4. Simulation and experimental results

### 4.1. Simulation results

#### 4.1.1. Simulation method

A finite element simulation method is developed to acquire time-domain signals under different stress states to explore the viability of the above methods. A three-dimensional solid model was utilized in the
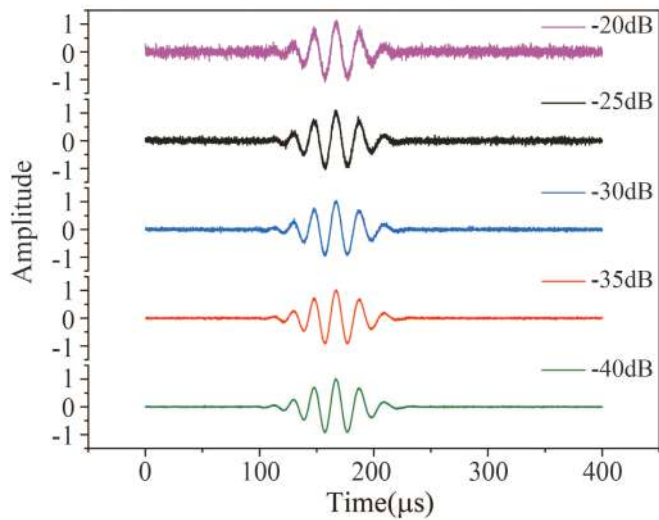
**Fig. 7.** A comparison of the signals under zero stress with five types of intensity noise.

simulation to establish an aluminum plate measuring 600 mm × 600 mm × 2 mm in dimensions. Poisson's ratio was 0.34. The density was 2730 kg/m³. Young's modulus was 73.1 GPa.

The whole simulation process comprises two analysis steps. The initial step uses the static analysis step to obtain the initial state under the action of pre-stress. The second step is using the dynamic explicit analysis step to analyze the propagation of Lamb waves. The excitation signal chosen was a Gabor pulse in Equation (8) with $A = 1$, $f_c =$

50 KHz, and $s = 20E-6$.

To generate a pure A0 mode, out-of-plane displacements in the same direction were simultaneously excited at two excitation nodes located at the same position on both surfaces of the aluminum plate, respectively. The out-of-plane displacement of a sensing node serves as the Lamb wave response signal. The distance between the excitation node and the sensing node is set as 300 mm.

In transient simulation, ensuring model accuracy hinges on two critical factors: grid size and time increment step. From experience, it is recommended that the grid size be a minimum of one-tenth of the Lamb wavelength. Considering the A0 mode with a wavelength of 34.68 mm at 50 KHz, the maximum grid size was restricted to 1 mm. The time increment step denotes the minimum time interval between each sub-analysis step. In this simulation, the time increment step was set to 5 ns. Fig. 12 shows the out-of-plane displacement field of the aluminum plate when the A0 wave reaches the sensing node at 100 MPa stress state.

Fig. 13 (a) displays the Lamb wave response signals received by sensing nodes under different stress states ranging from 0 to 100 MPa. With increasing stress, one can observe a gradual rise in the time delay of the time-domain signal envelope. Simultaneously, stress also changes the slope of TFSD (Fig. 13 (b)) and expands the time span of the wave packet gradually (Fig. 13 (c)). The trend of two time–frequency features changing with stress is the same as the theoretical prediction.

### 4.1.2. Calibration of simulation stress measurement expression

Lamb wave response signals obtained by finite element simulation can be represented by the dispersive wave packets model (i.e., Equation (12)). Thus, the wave packet parameter vector $\Theta = [\xi \delta \tau c \varphi]$ of Lamb wave response signals under all stress levels can be obtained by combining the expectation–maximization (EM) algorithm (detailed description in
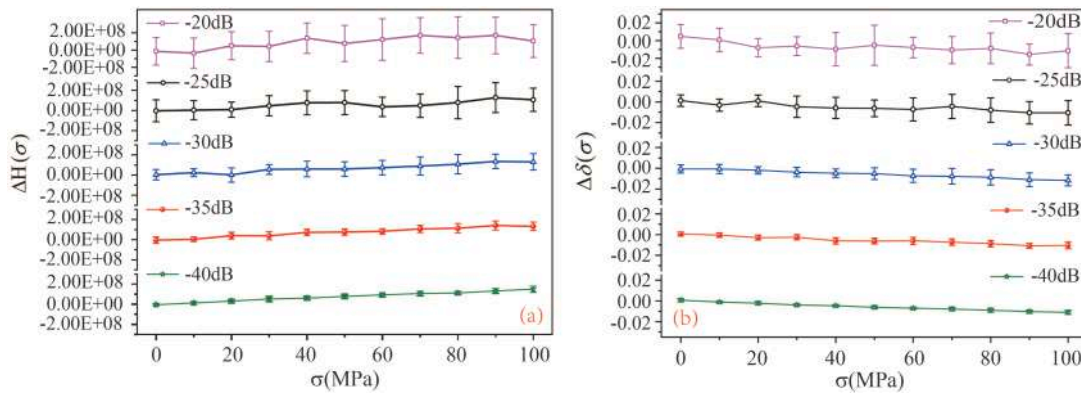


**Fig. 8.** The effect of different noise intensities on the linearity and standard deviation of proposed time–frequency characteristics: (a) and (b) the effect of noise on $\Delta H(\sigma)$ and $\Delta \delta(\sigma)$ respectively.
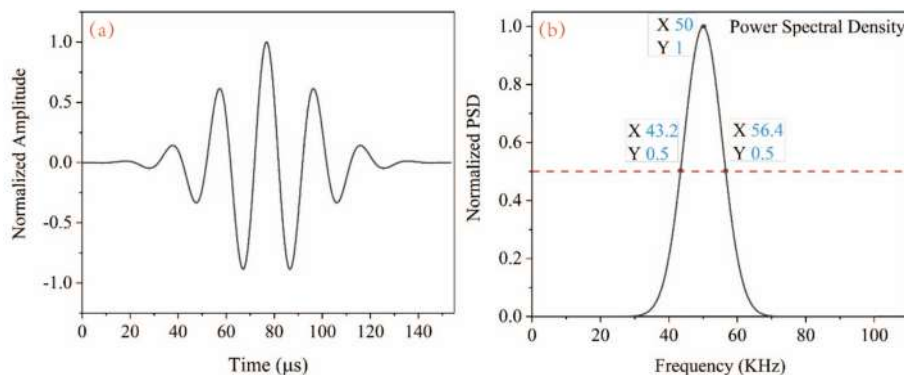


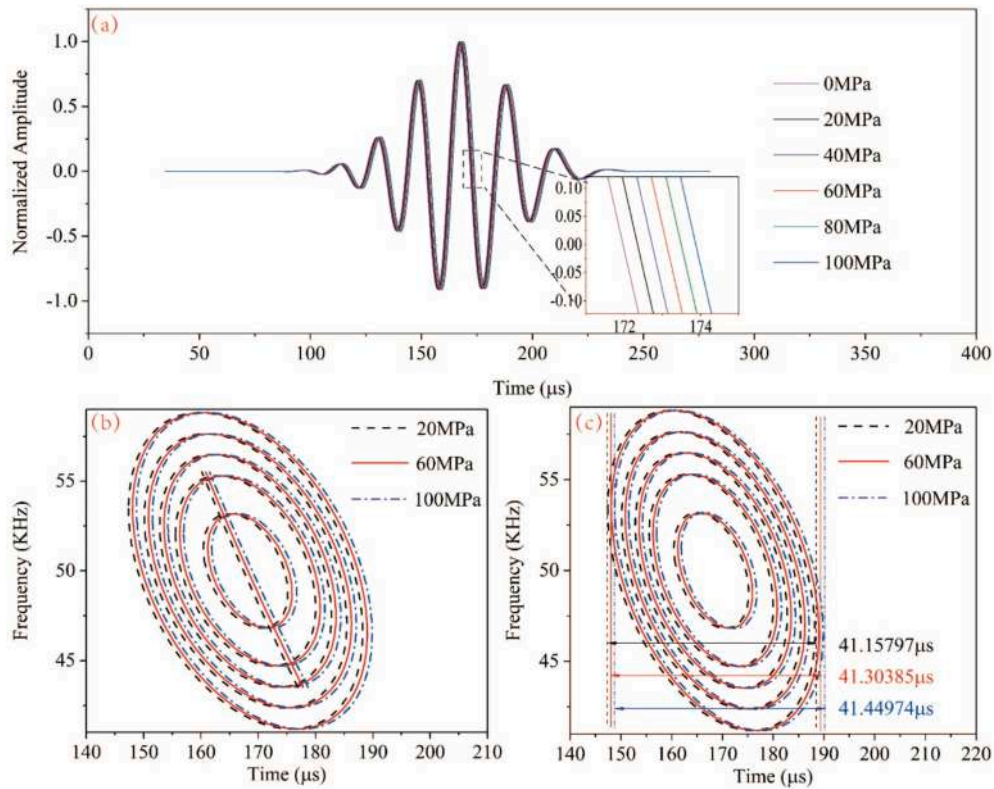**Fig. 9.** Excitation signal: (a) time-domain representation, (b) frequency-domain representation.

**Fig. 10.** Theoretical reconstruction waveforms and time–frequency feature of response signal under different stresses: (a) theoretically generated waveforms, (b) the slope of TFSD of the response signal, (c) the pulse width of the response signal.
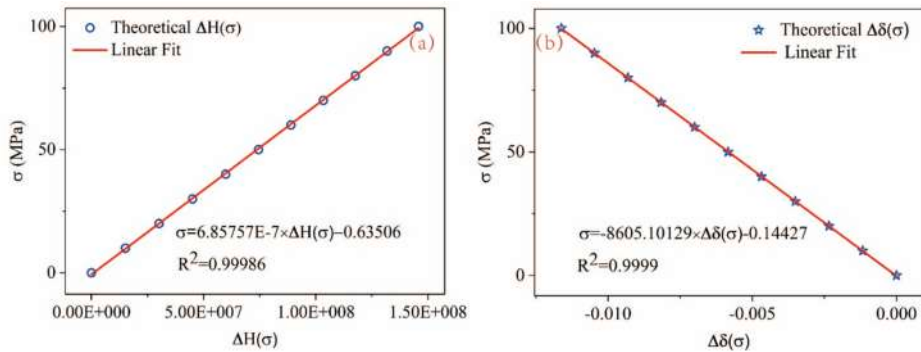


**Fig. 11.** Theoretical stress measurement expression: (a) expression of $\Delta H(\sigma)$, (b) expression of $\Delta\delta(\sigma)$.

Section 3.3) with the dispersive wave packets model. Furthermore, Substituting parameters $\delta$ and $c$ into Equation (20) yields the time-–frequency feature $H(\sigma)$.

The values of the packet parameter $\delta(\sigma)$, and $H(\sigma)$, corresponding to different stress states from 0 MPa to 100 MPa, are listed in Table 2.

The values of $\Delta H(\sigma)$ and $\Delta\delta(\sigma)$ for simulation response signals are calculated. The linear relationship between stress $\sigma$ and $\Delta H(\sigma)$ obtained by fitting is, namely, the stress measurement expression. Similarly, calculating the fitted linear relationship between stress $\sigma$ and $\Delta\delta(\sigma)$ means completing the calibration of the stress measurement expression regarding $\Delta\delta(\sigma)$. Fig. 14 shows the calibration results of two stress measurement factors based on simulation response signals.

An excellent linear correlation between the two stress measurement factors and stress is apparent. Fig. 14 (a) shows the stress measurement expression of simulated $\Delta H(\sigma)$

$$\sigma = 7.83001E - 7 \times \Delta H(\sigma) - 0.45778. \tag{29}$$

In Fig. 14 (b), the stress measurement expression of simulated $\Delta\delta(\sigma)$ is given

$$\sigma = -7381.65657 \times \Delta\delta(\sigma) - 1.28057. \tag{30}$$

### 4.2. Experimental results

#### 4.2.1. Experimental setup

To validate the practical applicability of the proposed method, two aluminum plates with different adhesives were used for the experiment. Fig. 15(a) and (b) depict the experimental setup and specimens. The specimen is 2024 aluminum, which is widely used in aviation. To avoid interference from boundary reflected waves on the first arrival wave, the aluminum plate dimensions are 800 mm × 600 mm × 2 mm (length × width × thickness). Each end of the plate has a 100 mm region reserved for connection to fixtures. The material properties include a density of 2730 kg/m$^3$, Poisson's ratio of 0.34, and Young's modulus of 73.1 GPa. Piezoelectric ceramic pieces (PZT) are used as actuators and response
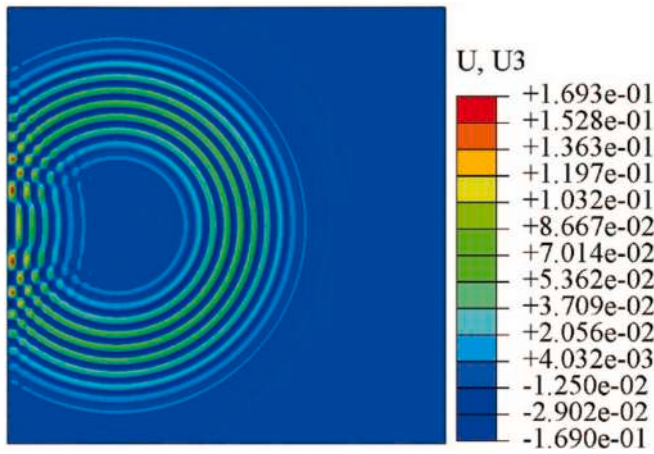
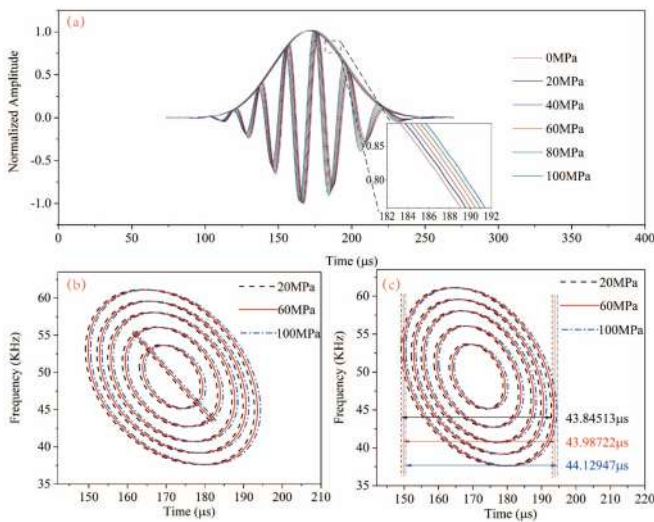**Fig. 12.** The out-of-plane displacement field.



**Fig. 13.** Finite element simulation waveforms and time–frequency feature of response signals under different stresses: (a) finite element simulation waveforms, (b) the slope of TFSD of response signals, (c) pulse width of response signals.

**Table 2**
The values of all parameters of finite element simulation response signals under all stress levels.

| | $\delta(\sigma)$ | $H(\sigma)$ |
|---|---|---|
| 0 MPa | 0.69582 | −3.71880E9 |
| 10 MPa | 0.69443 | −3.70681E9 |
| 20 MPa | 0.69293 | −3.69282E9 |
| 30 MPa | 0.69151 | −3.67916E9 |
| 40 MPa | 0.69007 | −3.66622E9 |
| 50 MPa | 0.68867 | −3.65322E9 |
| 60 MPa | 0.68746 | −3.64088E9 |
| 70 MPa | 0.68614 | −3.62927E9 |
| 80 MPa | 0.68473 | −3.61518E9 |
| 90 MPa | 0.68341 | −3.60222E9 |
| 100 MPa | 0.68246 | −3.59336E9 |

sensors. The material of piezoelectric ceramic pieces is PZT-5H. Its diameter and thickness are 10 mm and 0.2 mm, respectively. We used two types of adhesives to stick the PZT onto the tested aluminum plate, shown in Fig. 15 (c). These adhesives are dual-component epoxy adhesive (J-133 structure adhesive, produced by the Institute of Petrochemistry Heilongjiang Academy of Sciences) and epoxy prepreg

(Carbon fiber reinforced epoxy prepreg). Four PZTs are pasted onto the aluminum plate. PZT1 and PZT2 are pasted on both sides of the excitation point to excite Lamb wave signals, as shown in Fig. 15 (d). The double-sided excitation method can remove S0 mode Lamb waves, and generate a pure A0 wave in the aluminum plate. PZT3 and PZT4 are pasted on both sides of the sensing point to receive Lamb wave signals. The excitation point and sensing point located on the axis of symmetry of the aluminum plate form a pitch-catch path with a distance of 300 mm. The pitch-catch path is parallel to the direction of loading. A set of electronic equipment systems is used to excite and obtain Lamb wave signals, including an analog output module (PCI-1721), a high-voltage amplifier (ATA-2022), and an oscilloscope (DSO5034A). The control program is realized using LabVIEW.

A self-designed fixture is used to connect the aluminum plate to the stretching machine, which ensures that static uniaxial tensile load is evenly applied to the aluminum plate. The lower end of the fixture has a 600 mm × 2 mm × 100 mm groove in the middle. One end of the aluminum plate is inserted into the groove to fully match the fixture, and each end is fixed with 58 dowel pins with a diameter of $\phi$10.

The assembled fixture and aluminum plate are clamped at both ends of the tensile testing machine (Sinter-WEW-B-1000 KN)'s hydraulic grips for tensile testing. There are eight stress levels ranging from 30 MPa to 100 MPa, with increments of 10 MPa. After reaching a stress level, hold for 1 min to stabilize the applied stress. Then, the pulse signal in Fig. 11 is generated through an analog output module. The amplitude of the pulse signal is ±5 V. To enhance the signal-to-noise ratio, the pulse signal undergoes amplification through a high-voltage amplifier and is subsequently powered by the driver. The gain of the voltage amplifier is set to 15 dB. Meanwhile, the oscilloscope begins to collect dynamic data from the response sensors. The sampling rate is set to 2 MSamples/s, and to reduce the impact of noise on the signal, 32 times averaging sampling is adopted. Finally, the signals are stored in a computer for signal processing.

*4.2.2. Experimental results and the effects of adhesive types*

Lamb wave response signals propagated along the direction of loading under different stress states are shown in Fig. 16 (a). The slope of TFSD and time-domain width of the wave packet of experimental response signals at 30 MPa, 60 MPa, and 90 MPa are illustrated in Fig. 16 (b) and (c), respectively. It is evident that the trend of two time–frequency features changing with stress is the same as theoretical prediction and finite element simulation.

The pulse width impact factor $\delta(\sigma)$ and wave packet parameter $c$ of the experimental response signals under all stress levels can be estimated by combining the EM algorithm with the dispersive wave packet model. Substituting $\delta(\sigma)$ and $c$ into Equation (20) can obtain the slope of TFSD $H(\sigma)$ under all stress levels. To verify the stability of the proposed method, the specimen bonded with each type of adhesive was subjected to three tensile tests at different times within one day respectively. Each test collected one set of data, and we can obtain three sets of results based on each specimen. $H(\sigma)$ and $\delta(\sigma)$ obtained from experimental signals of dual-component epoxy adhesive specimens are shown in Table 3.

We consider the 0 MPa state as the initial state. The values of $H(\sigma = 0)$ and $\delta(\sigma = 0)$ can be obtained by fitting the experimental data. Thus, experimental $\Delta H(\sigma)$ and $\Delta\delta(\sigma)$ under all stress states of each test can be obtained by Equation (21) and Equation (23).

The relation between these two stress measurement factors of two aluminum plates with different adhesives and stress are displayed in Fig. 17 (a) and (b). The scatter points represent three sets of results for each specimen. The symbol represents the mean of three sets of $\Delta H(\sigma)$ or $\Delta\delta(\sigma)$ under every stress state. The error bar represents the standard deviation. It can be seen that the variation trends of the experimental $\Delta H(\sigma)$ and $\Delta\delta(\sigma)$ every type of adhesive sample with stress are different. This means that the coefficients for stress evaluation based on two time–frequency characteristics change with different adhesives.
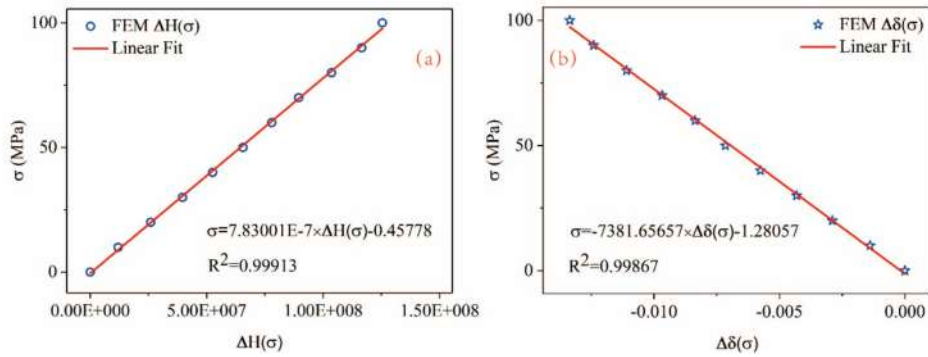
**Fig. 14.** Simulation stress measurement expression: (a) expression of $\Delta H(\sigma)$, (b) expression of $\Delta\delta(\sigma)$.
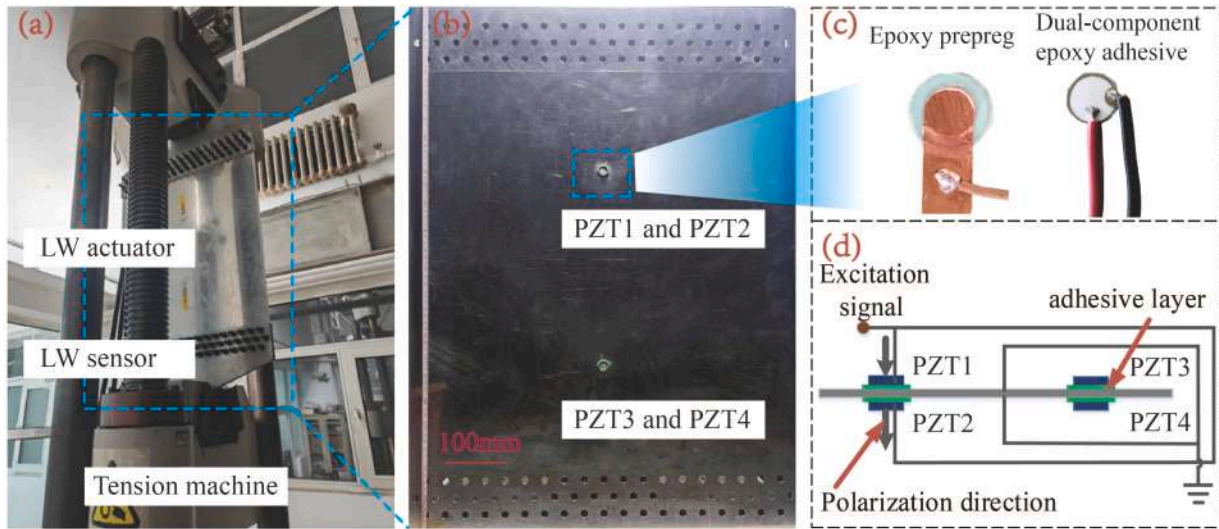


**Fig. 15.** Experimental setup: (a) experimental process, (b) experimental specimen, (c) two types of stick Methods of PZT, (d) diagrammatic sketch of double-sided excitation method.

Furthermore, regarding the time–frequency characteristic $H(\sigma)$, the linearity and standard deviation of the experimental results of the dual-component epoxy adhesive specimens are significantly better than epoxy prepreg adhesive specimens. Therefore, using the dual-component epoxy adhesive to bond PZT is more conducive to stress evaluation based on the time–frequency characteristic $H(\sigma)$. As for the time–frequency characteristic $\delta(\sigma)$, the linearity and standard deviation of the experimental results for the two different adhesive specimens are relatively good. Therefore, from the perspective of linearity and standard deviation, the relationship between $\delta(\sigma)$ and stress is more stable than that of $H(\sigma)$, implying that $\delta(\sigma)$ is a superior stress evaluation characteristic.

The comparison of the stress measurement factor $\Delta H(\sigma)$ and $\Delta\delta(\sigma)$ of theory, simulation, and experiment is also displayed in Fig. 17. The simulation results are close to the theoretical results. However, the slope obtained from the experimental results is considerably different from the theoretical slope. We can see that the type of adhesive has a significant impact on the slope of the experiment results. Therefore, it can be inferred that one significant reason for the discrepancy between experiment and theory is the lack of the influence of the adhesive types on two time–frequency characteristics in theory or simulation.

### 4.3. Actual stress measurement

By calibrating stress measurement coefficients through experiments, stress evaluation can be achieved. Due to the superior linearity and

stability of the data compared to that of the epoxy prepreg, we chose the experimental data of the dual-component epoxy adhesive specimen for the calibration of stress measurement expression. By fitting the mean of three sets of $\Delta H(\sigma)$ or $\Delta\delta(\sigma)$ under every stress state of dual-component epoxy adhesive specimen, as shown in Fig. 17 (a) and (b), the experimental stress measurement expression representing the relationship between stress $\sigma$ and stress measurement factor $\Delta H(\sigma)$ can be calibrated. The calibration result is shown in Fig. 18 (a)

$$\sigma = 1.43233E - 6 \times \Delta H(\sigma) + 0.67354. \tag{31}$$

The experimental stress measurement expression representing the relationship between stress $\sigma$ and stress measurement factor $\Delta\delta(\sigma)$ can be calibrated, as shown in Fig. 18 (b)

$$\sigma = -5481.61385 \times \Delta\delta(\sigma) - 0.36408. \tag{32}$$

The determination coefficients for the linear fitting exceed 0.98, indicating an excellent linear correlation between the two stress measurement factors obtained from the experimental results and the applied stress.

After obtaining the experimental stress measurement expression, three uniaxial tensile tests were conducted on the identical batch of specimens to validate the efficacy of the proposed method. The applied stress on the tested aluminum plate changes from 35 to 95 MPa with increments of 10 MPa. Three sets of response signals were collected for stress evaluation. Stress measurement factors $\Delta H(\sigma)$ and $\Delta\delta(\sigma)$ are listed in Table 4.
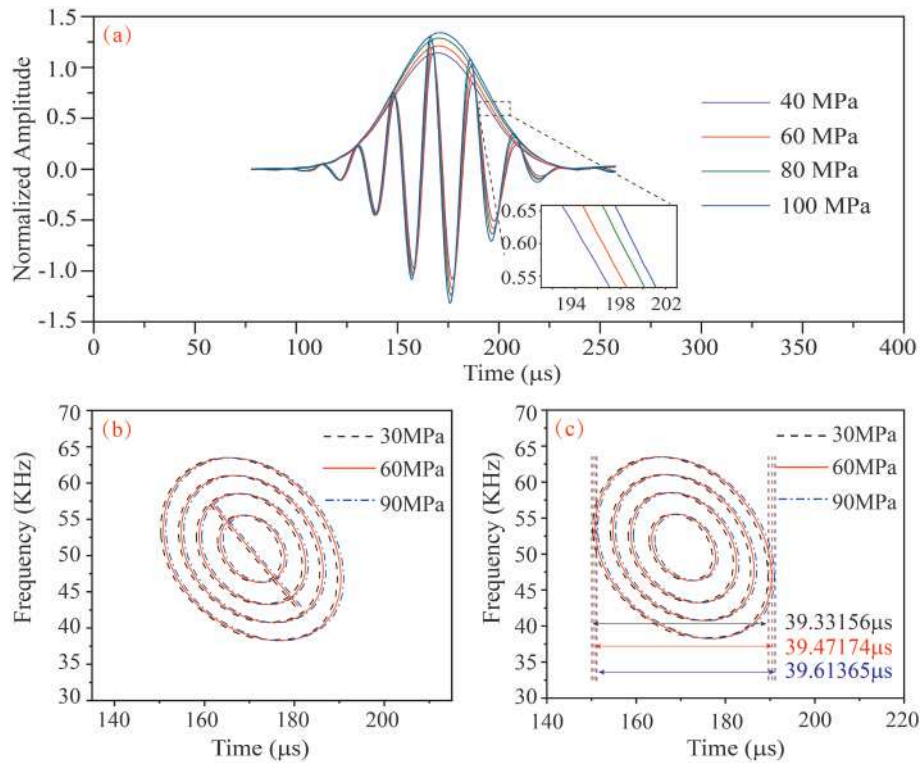
**Fig. 16.** Experimental waveforms and time–frequency feature of response signal under different stresses: (a) experimental response waveforms, (b) the slope of TFSD of experimental response signals, (c) pulse width of experimental response signals.

**Table 3**
Three sets of results of the dual-component epoxy adhesive specimen.

| Stress (MPa) | $H(\sigma)(10^9)$ | | | $\delta(\sigma)$ | | |
|---|---|---|---|---|---|---|
| | Test 1 | Test 2 | Test 3 | Test 1 | Test 2 | Test 3 |
| 30 | −4.64809 | −4.65224 | −4.65319 | 0.82775 | 0.82780 | 0.82780 |
| 40 | −4.64571 | −4.64483 | −4.65517 | 0.82598 | 0.82617 | 0.82697 |
| 50 | −4.63334 | −4.64148 | −4.64413 | 0.82415 | 0.82399 | 0.82483 |
| 60 | −4.62857 | −4.63369 | −4.64053 | 0.82288 | 0.82280 | 0.82352 |
| 70 | −4.62521 | −4.6288E9 | −4.62880 | 0.82035 | 0.82137 | 0.82121 |
| 80 | −4.61766 | −4.61838 | −4.61838 | 0.81830 | 0.81882 | 0.81884 |
| 90 | −4.60882 | −4.61505 | −4.61735 | 0.81639 | 0.81756 | 0.81732 |
| 100 | −4.60479 | −4.60499 | −4.60016 | 0.81532 | 0.81549 | 0.81517 |

Stress measurement factors $\Delta H(\sigma)$ and $\Delta\delta(\sigma)$ were substituted into Equation (31) and Equation (32) to obtain the estimated stress. Table 5 lists the evaluation results using the stress measurement factor from Table 4.

The maximum evaluated deviation for $\Delta H(\sigma)$ in Table 5 is 15.44195 MPa, and for $\Delta\delta(\sigma)$, the maximum evaluated deviation is 5.49768 MPa. The error bar diagrams for three sets of evaluation results are shown in Fig. 19. The maximum standard deviation of three measured stresses based on $\Delta\delta(\sigma)$ is 3.76433 MPa, demonstrating excellent measurement stability. The maximum standard deviation of three measured stresses based on $\Delta H(\sigma)$ is 9.12492 MPa. Similarly, it can be seen that the stress evaluation performance of $\delta(\sigma)$ is superior to $H(\sigma)$.

The results show that the stress evaluation expressions (Equation (31) and Equation (32)) calibrated from the experimental data work well for stress measurement.

In practice, once the suitable pitch-catch distance has been selected, the stress evaluation expressions can be calibrated as long as time–frequency characteristics of signals under any two known stress levels are obtained. Then, actual stress levels can be measured based on calibrated stress evaluation expressions. It should be clarified that stress evaluation expression varies with the propagation distance, which has

implications for the convenience of the proposed method. Therefore, we will explore characteristics that are insensitive to propagation distance in the next work. In addition, the uniaxial load direction is predetermined in this work, ensuring alignment with the propagation path of Lamb waves. However, during actual stress measurement, maintaining parallelism between the stress direction and the pitch-catch path poses a challenge when employing a pair of actuator-receiver sensors. The transducer array, similar to a three-dimensional rosette gauge, needs to be set to calculate the stress in any desired direction by utilizing information from various directions.

## 5. Conclusion

This paper proposes a stress measurement strategy based on time–frequency characteristics. Firstly, two time–frequency characteristics of the signals are selected for stress measurement. One is the slope of TFSD ($H(\sigma)$), and the other is the pulse width impact factor ($\delta(\sigma)$). The theoretical expression of the slope of TFSD is derived. The theoretical predicted values of these two time–frequency characters demonstrate a linear relationship with uniaxial stress. Therefore, they promise to serve as the features for stress evaluation. To better utilize the methods pro-
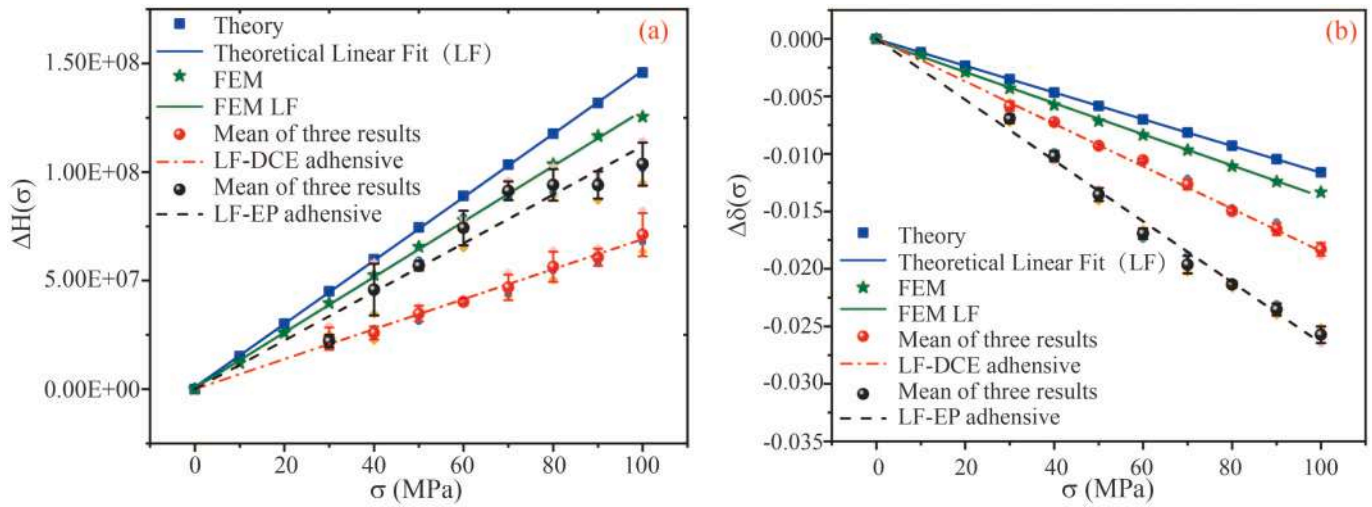
**Fig. 17.** The comparison of the stress measurement factor $\Delta H(\sigma)$ and $\Delta\delta(\sigma)$ of theory, simulation, and experiment (dual-component epoxy (DCE) adhesive and epoxy prepreg (EP) adhesive): (a) the comparison of $\Delta H(\sigma)$; (b) the comparison of $\Delta\delta(\sigma)$.
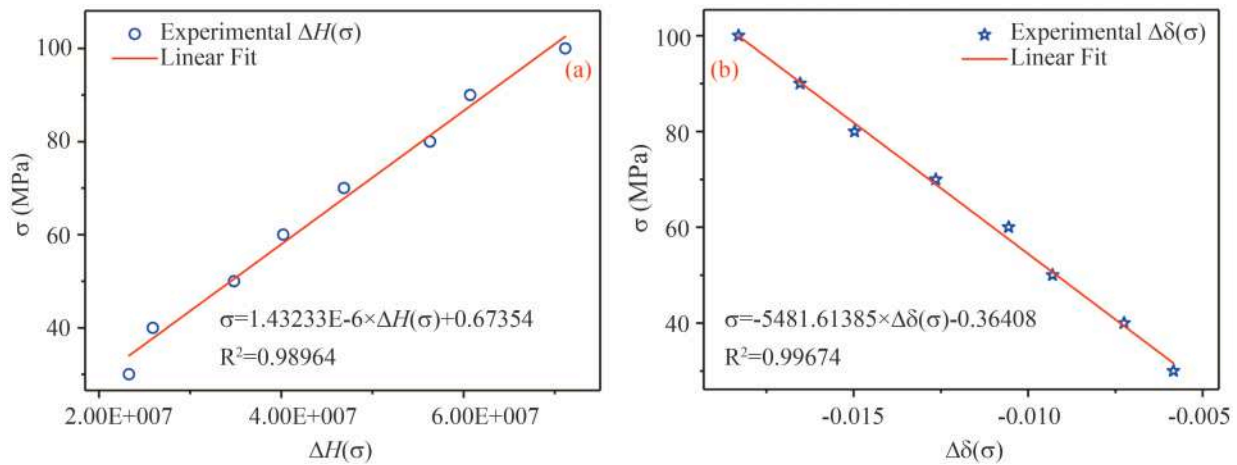


**Fig. 18.** Experimental stress measurement expression: (a) expression of $\Delta H(\sigma)$, (b) expression of $\Delta\delta(\sigma)$.

**Table 4**
Stress measurement factors calculated from three uniaxial tensile tests.

| Applied Stress (MPa) | $\Delta H(\sigma)(10^7)$ | | | $\Delta\delta(\sigma)$ | | |
|---|---|---|---|---|---|---|
| | Test 1 | Test 2 | Test 3 | Test 1 | Test 2 | Test 3 |
| 35 | 2.15030 | 2.20911 | 2.51431 | −0.00682 | −0.00574 | −0.00674 |
| 45 | 3.03490 | 3.40523 | 3.54618 | −0.00855 | −0.00837 | −0.00826 |
| 55 | 3.85313 | 3.66334 | 4.41227 | −0.01076 | −0.00986 | −0.01027 |
| 65 | 4.02563 | 4.24217 | 5.16887 | −0.01154 | −0.01150 | −0.01231 |
| 75 | 4.94020 | 5.36857 | 6.19359 | −0.01341 | −0.01436 | −0.01475 |
| 85 | 5.32704 | 5.93364 | 6.3016 | −0.01552 | −0.01538 | −0.01628 |
| 95 | 6.91784 | 6.89002 | 7.66363 | −0.01754 | −0.01745 | −0.01767 |

posed in this paper, the impacts of excitation signal parameters (i.e., bandwidth and center frequency) and noise on two time–frequency characteristics were discussed through theoretical analysis.

Meanwhile, the viability of the proposed method was investigated from three aspects: theory, simulation, and experiment. Their results all demonstrate that the proposed time–frequency characteristics have a good linear relationship with uniaxial stress. The slope of the simulation results is close to the theoretical slope. The slope obtained from the experimental results is considerably different from the theoretical slope. To investigate the reason for the discrepancy between the experiment and theory, aluminum plate specimens with two different types of ad-

hesives were used for the experiment. The variation trends of experimental $\Delta H(\sigma)$ and $\Delta\delta(\sigma)$ every type of adhesive sample with stress are different. It can be inferred that one significant reason for the discrepancy between experiment and theory is the lack of the influence of the adhesive types on two time–frequency characteristics in theory or simulation. In addition, from the perspective of linearity and standard deviation, the relationship between $\delta(\sigma)$ and stress is more stable than that of $H(\sigma)$, implying that $\delta(\sigma)$ is a superior stress evaluation characteristic. Then, according to the stress evaluation expression, three uni-axial tensile tests in the range of 35–95 MPa were conducted on the identical batch of specimens. The maximum standard deviation of three

**Table 5**

Stress measurements using the stress measurement factor from Table 4.

| Actual Stress (MPa) | Measured stress of $H(\sigma)$ (MPa) | | | Measured stress of $\delta(\sigma)$ (MPa) | | |
|---|---|---|---|---|---|---|
| | Test 1 | Test 2 | Test 3 | Test 1 | Test 2 | Test 3 |
| 35 | 31.47298 | 32.31535 | 36.68674 | 37.01680 | 31.10675 | 36.56217 |
| 45 | 44.14333 | 49.44766 | 51.46661 | 46.49903 | 45.52015 | 44.90178 |
| 55 | 55.86313 | 53.14468 | 63.87181 | 58.63663 | 53.68117 | 55.92171 |
| 65 | 58.33381 | 61.43544 | 74.70885 | 62.86809 | 62.68441 | 67.10814 |
| 75 | 71.43355 | 77.56925 | 89.3862 | 73.16907 | 78.32641 | 80.49768 |
| 85 | 76.97439 | 85.66284 | 90.93325 | 84.73367 | 83.96549 | 88.88229 |
| 95 | 99.75983 | 99.36143 | 110.44195 | 95.78643 | 95.27374 | 96.49852 |
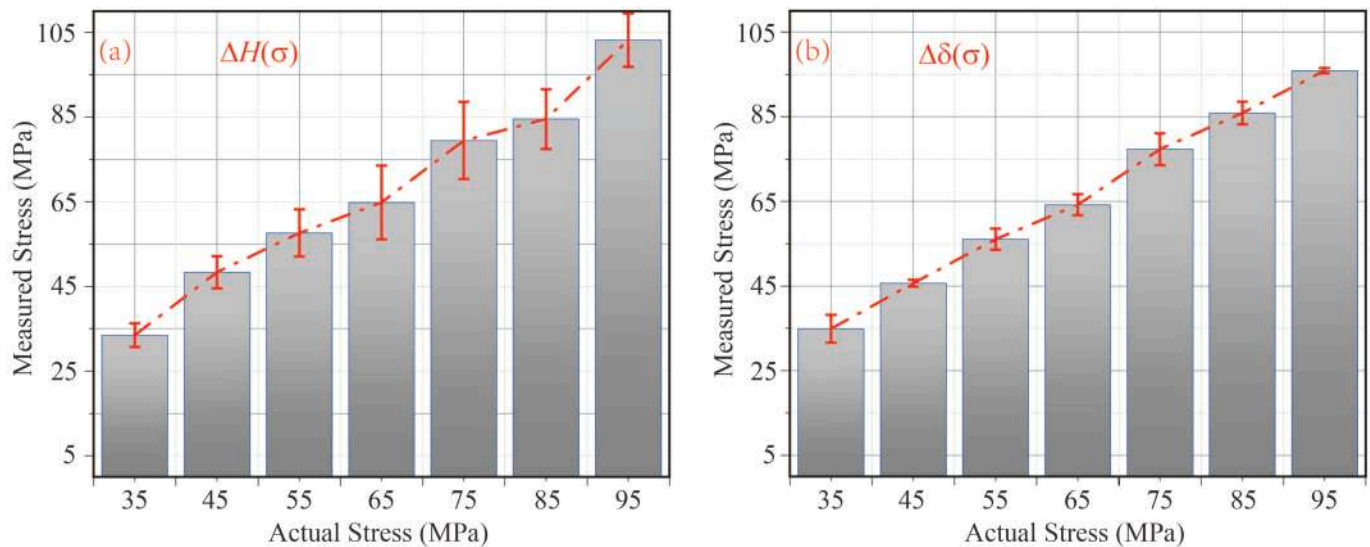


**Fig. 19.** The error bar diagrams for three sets of evaluation results: (a) and (b) three measured stresses based on $\Delta H(\sigma)$ and $\Delta \delta(\sigma)$ respectively.

measured stresses based on $\Delta \delta(\sigma)$ is 3.76433 MPa, demonstrating excellent measurement stability. The maximum standard deviation of three measured stresses based on $\Delta H(\sigma)$ is 9.12492 MPa.

This paper fully utilizes the information in the Lamb wave signals and introduces a new way of detecting stress based on two time–frequency characteristics. The proposed method is adaptable for integration into current health monitoring systems to enrich stress monitoring strategy.

**CRediT authorship contribution statement**

**Hexin Cui:** Writing – review & editing, Writing – original draft, Methodology, Investigation, Conceptualization. **Zhichun Zhang:** Visualization, Investigation, Formal analysis, Conceptualization. **Hongbo Jia:** Visualization, Methodology, Investigation, Formal analysis. **Jiaze He:** Writing – review & editing, Supervision, Methodology, Conceptualization. **Yanju Liu:** Writing – review & editing, Supervision, Methodology, Investigation, Conceptualization. **Jinsong Leng:** Writing – review & editing, Supervision.

**Declaration of competing interest**

The authors declare that they have no known competing financial interests or personal relationships that could have appeared to influence the work reported in this paper.

**Data availability**

Data will be made available on request.

**References**

[1] C. Wang, X. Wang, X. Zhou, Z. Li, The aircraft skin crack inspection based on different-source sensors and support vector machines, J. Nondestr. Eval. 35 (2016) 46, https://doi.org/10.1007/s10921-016-0359-3.

[2] X.L. Qing, Y.L. Liao, Y.H. Wang, B.Q. Chen, F.H. Zhang, Y.S. Wang, Machine learning based quantitative damage monitoring of composite structure, Int. J. Smart Nano Mater. 13 (2022) 167–202, https://doi.org/10.1080/19475411.2022.2054878.

[3] D.C. Ji, F. Gao, J.D. Hua, J. Lin, Quantitative evaluation of crack based on the sparse decomposition of array Lamb wave propagation, Ultrasonics 134 (2023) 107101, https://doi.org/10.1016/j.ultras.2023.107101.

[4] H. Yang, Y. Huang, Z. Zhou, J. Ou, Long-term performance of packaged fiber Bragg grating sensors for strain monitoring inside creep medium, Int. J. Smart Nano Mater. 13 (2022) 42–63, https://doi.org/10.1080/19475411.2022.2027548.

[5] B.Q. Wang, W.J. Shi, B. Zhao, J.B. Tan, Ultrasonics methodology for defect and stress detection of in-serviced T-shaped R-zone components, Ultrasonics 124 (2022) 106730, https://doi.org/10.1016/j.ultras.2022.106730.

[6] Z. Zhang, M.L. Liu, Y.Z. Liao, Z.Q. Su, Y. Xiao, Contact acoustic nonlinearity (CAN)-based continuous monitoring of bolt loosening: Hybrid use of high-order harmonics and spectral sidebands, Mech. Syst. Signal Proc. 103 (2018) 280–294, https://doi.org/10.1016/j.ymssp.2017.10.009.

[7] N.S. Rossini, M. Dassisti, K.Y. Benyounis, A.G. Olabi, Methods of measuring residual stresses in components, Mater. Des. 35 (2012) 572–588, https://doi.org/10.1016/j.matdes.2011.08.022.

[8] W. Shi, J. Li, B. Zhao, J. Tan, A baseline-free stress monitoring strategy based on acoustoelastic Lamb waves using PWAS array, Struct. Health Monit. 22 (2022) 1745–1759, https://doi.org/10.1177/14759217221115849.

[9] X. Li, H. Liu, X. Chen, Y. Lyu, Z. Liu, Inverse of initial stress in carbon fiber reinforced polymer laminates using Lamb waves and deep neural network, Ultrasonics 132 (2023) 107005, https://doi.org/10.1016/j.ultras.2023.107005.

[10] D.S. Hughes, J.L. Kelly, Second-order elastic deformation of solids, Phys. Rev. 92 (1953) 1145, https://doi.org/10.1103/PhysRev.92.1145.

[11] W. Wang, C.H. Xu, Y.M. Zhang, Y.F. Zhou, S.H. Meng, Y. Deng, An improved ultrasonic method for plane stress measurement using critically refracted longitudinal waves, NDT and E Int. 99 (2018) 117–122, https://doi.org/10.1016/j.ndteint.2018.07.006.

[12] K. Okada, Acoustoelastic determination of stress in slightly orthotropic materials: a method based on the effect of stress-induced acoustic birefringence is described to determine stresses in a rolled plate under the state of plane stress, Exp. Mech. 21 (1981) 461–466, https://doi.org/10.1007/BF02327418.

[13] K.-Y. Jhang, H.-H. Quan, J. Ha, N.-Y.-J.-U. Kim, Estimation of clamping force in high-tension bolts through ultrasonic velocity measurement, Ultrasonics 44 (2006) e1339–e1342, https://doi.org/10.1016/j.ultras.2006.05.190.

[14] Y. Javadi, M. Hasani, S. Sadeghi, Investigation of clamping effect on the welding sub-surface residual stress and deformation by using the ultrasonic stress measurement and finite element method, J. Nondestr. Eval. 34 (2015) 3, https://doi.org/10.1007/s10921-015-0277-9.

[15] H.B. Liu, Y.P. Li, T. Li, X. Zhang, Y.K. Liu, K. Liu, Y.Q. Wang, Influence factors analysis and accuracy improvement for stress measurement using ultrasonic longitudinal critically refracted (LCR) wave, Appl. Acoust. 141 (2018) 178–187, https://doi.org/10.1016/j.apacoust.2018.07.017.

[16] S.M. Yang, M.Q. Wang, L. Yang, Investigation of uncertain factors on measuring residual stress with critically refracted longitudinal waves, Appl. Sci.-Basel 9 (2019) 485, https://doi.org/10.3390/app9030485.

[17] J.B. He, Z.H. Li, J. Teng, M. Li, Y. Wang, Absolute stress field measurement in structural steel members using the Lcr wave method, Measurement 122 (2018) 679–687, https://doi.org/10.1016/j.measurement.2018.03.022.

[18] O.R. Gericke, Determination of the geometry of hidden defects by ultrasonic pulse analysis testing, J. Acoust. Soc. Am. 35 (1963) 364–368, https://doi.org/10.1121/1.1918471.

[19] J. Blinka, W. Sachse, Application of ultrasonic-pulse-spectroscopy measurements to experimental stress analysis: ultrasonic-pulse-spectroscopy measurements are used to measure the stress-induced interference effects between two shear waves propagating in uniaxially deformed specimens of aluminum, Exp. Mech. 16 (1976) 448–453, https://doi.org/10.1007/BF02324101.

[20] Z.H. Li, J.B. He, D.K. Liu, N.X. Liu, Z.L. Long, J. Teng, Influence of uniaxial stress on the shear-wave spectrum propagating in steel members, Sensors 19 (2019) 492, https://doi.org/10.3390/s19030492.

[21] D. Husson, A perturbation theory for the acoustoelastic effect of surface waves, J. Appl. Phys. 57 (1985) 1562–1568, https://doi.org/10.1063/1.334471.

[22] N. Gandhi, J.E. Michaels, S.J. Lee, Acoustoelastic Lamb wave propagation in a homogeneous, isotropic aluminum plate, in: 37th Annual Review of Progress in Quantitative Nondestructive Evaluation (QNDE), San Diego, CA, Vol. 1335, 2010, pp. 161–168, doi: 10.1063/1.3591852.

[23] N. Gandhi, J.E. Michaels, S.J. Lee, Acoustoelastic Lamb wave propagation in biaxially stressed plates, J. Acoust. Soc. Am. 132 (2012) 1284–1293, https://doi.org/10.1121/1.4740491.

[24] L. Qiu, X.X. Yan, X.D. Lin, S.F. Yuan, Multiphysics simulation method of Lamb wave propagation with piezoelectric transducers under load condition, Chin. J. Aeronaut. 32 (2019) 1071–1086, https://doi.org/10.1016/j.cja.2019.02.007.

[25] C. Cheng, H.F. Mei, V. Giurgiutiu, S.F. Yuan, F. Fang, R. James, Simulation of guided wave under varying temperature and load conditions, in: Conference on Health Monitoring of Structural and Biological Systems IX, Electr Network, 2020, p. 11381, https://doi.org/10.1117/12.2559702.

[26] W.J. Shi, J.X. Li, B. Zhao, J.B. Tan, An online stress monitoring strategy based on Wigner-Ville time-frequency energy extraction of single-frequency dual mode Lamb waves, Measurement 200 (2022) 111600, https://doi.org/10.1016/j.measurement.2022.111600.

[27] F. Shi, J.E. Michaels, S.J. Lee, In situ estimation of applied biaxial loads with Lamb waves, J. Acoust. Soc. Am. 133 (2013) 677–687, https://doi.org/10.1121/1.4773867.

[28] N. Pei, L.J. Bond, Comparison of acoustoelastic Lamb wave propagation in stressed plates for different measurement orientations, J. Acoust. Soc. Am. 142 (2017) EL327–EL331, https://doi.org/10.1121/1.5004388.

[29] P.W. Loveday, C.S. Long, P.D. Wilcox, Semi-analytical finite element analysis of the influence of axial loads on elastic waveguides, in: Finite Element Analysis-From Biomedical Applications to Industrial Developments, IntechOpen, 2012, pp. 439–454, doi: 10.5772/38609.

[30] K. Peddeti, S. Santhanam, Dispersion curves for Lamb wave propagation in prestressed plates using a semi-analytical finite element analysis, J. Acoust. Soc. Am. 143 (2018) 829–840, https://doi.org/10.1121/1.5023335.

[31] Y.L. Ma, Z.Y. Yang, J.Q. Zhang, K.H. Liu, Z.J. Wu, S.Y. Ma, Axial stress monitoring strategy in arbitrary cross-section based on acoustoelastic guided waves using PZT sensors, AIP Adv. 9 (2019) 125304, https://doi.org/10.1063/1.5130723.

[32] A. Abderahmane, A. Lhemery, L. Daniel, Effects of multiaxial pre-stress on Lamb and shear horizontal guided waves (vol 149, pg 1724, 2021), J. Acoust. Soc. Am. 151 (2022) 3315, https://doi.org/10.1121/10.0011422.

[33] P. Zuo, X.D. Yu, Z. Fan, Acoustoelastic guided waves in waveguides with arbitrary prestress, J. Sound Vibrat. 469 (2020) 115113, https://doi.org/10.1016/j.jsv.2019.115113.

[34] M.L. Liu, W.Y. Zhang, X. Chen, L. Li, K. Wang, H. Wang, F.S. Cui, Z.Q. Su, Modelling guided waves in acoustoelastic and complex waveguides: from SAFE theory to an open-source tool, Ultrasonics 136 (2024) 107144, https://doi.org/10.1016/j.ultras.2023.107144.

[35] H.J. Lim, H. Sohn, Online stress monitoring technique based on Lamb-wave measurements and a convolutional neural network under static and dynamic loadings, Exp. Mech. 60 (2020) 171–179, https://doi.org/10.1007/s11340-019-00546-8.

[36] P.F. Pai, H.G. Deng, M.J. Sundaresan, Time-frequency characterization of Lamb waves for material evaluation and damage inspection of plates, Mech. Syst. Signal Proc. 62–63 (2015) 183–206, https://doi.org/10.1016/j.ymssp.2015.03.011.

[37] J.D. Hua, X.W. Cao, Y.G. Yi, J. Lin, Time-frequency damage index of Broadband Lamb wave for corrosion inspection, J. Sound Vibrat. 464 (2020) 114985, https://doi.org/10.1016/j.jsv.2019.114985.

[38] S.H.M. Rizvi, M. Abbas, An advanced Wigner-Ville time-frequency analysis of Lamb wave signals based upon an autoregressive model for efficient damage inspection, Measur. Sci. Technol. 32 (2021) 095601, https://doi.org/10.1088/1361-6501/abef3c.

[39] H. Jia, Z. Zhang, H. Liu, F. Dai, Y. Liu, J. Leng, An approach based on expectation-maximization algorithm for parameter estimation of Lamb wave signals, Mech. Syst. Signal Proc. 120 (2019) 341–355, https://doi.org/10.1016/j.ymssp.2018.10.020.